LETTER

https://doi.org/10.1038/s41586-018-0414-6

RNA velocity of single cells

Gioele La Manno[1,2], Ruslan Soldatov[3], Amit Zeisel[1,2], Emelie Braun[1,2], Hannah Hochgerner[1,2], Viktor Petukhov[3,4], Katja Lidschreiber[5], Maria E. Kastriti[6], Peter Lönnerberg[1,2], Alessandro Furlan[1], Jean Fan[3], Lars E. Borm[1,2], Zehua Liu[3], David van Bruggen[1], Jimin Guo[3], Xiaoling He[7], Roger Barker[7], Erik Sundström[8], Gonçalo Castelo-Branco[1], Patrick Cramer[5,9], Igor Adameyko[6], Sten Linnarsson[1,2]* & Peter V. Kharchenko[3,10]*

RNA abundance is a powerful indicator of the state of individual cells. Single-cell RNA sequencing can reveal RNA abundance with high quantitative accuracy, sensitivity and throughput[1]. However, this approach captures only a static snapshot at a point in time, posing a challenge for the analysis of time-resolved phenomena such as embryogenesis or tissue regeneration. Here we show that RNA velocity—the time derivative of the gene expression state—can be directly estimated by distinguishing between unspliced and spliced mRNAs in common single-cell RNA sequencing protocols. RNA velocity is a high-dimensional vector that predicts the future state of individual cells on a timescale of hours. We validate its accuracy in the neural crest lineage, demonstrate its use on multiple published datasets and technical platforms, reveal the branching lineage tree of the developing mouse hippocampus, and examine the kinetics of transcription in human embryonic brain. We expect RNA velocity to greatly aid the analysis of developmental lineages and cellular dynamics, particularly in humans.

During development, differentiation occurs on a timescale of hours to days, which is comparable to the typical half-life of mRNA. The relative abundance of nascent (unspliced) and mature (spliced) mRNA can be exploited to estimate the rates of gene splicing and degradation, without the need for metabolic labelling, as previously shown in bulk[2–4]. We reasoned that similar signals may be detectable in single-cell RNA sequencing (RNA-seq) data, and could reveal the rate and direction of change of the entire transcriptome during dynamic processes.

All common single-cell RNA-seq protocols rely on oligo-dT primers to enrich for polyadenylated mRNA molecules. Nevertheless, examining single-cell RNA-seq datasets based on the SMART-seq2, STRT/C1, inDrop and 10x Genomics Chromium protocols[5–8], we found that 15–25% of reads contained unspliced intronic sequences (Fig. 1a), in agreement with previous observations in bulk[4] (14.6%) and single-cell[5] (~20%) RNA-seq. Most such reads originated from secondary priming positions within the intronic regions (Extended Data Fig. 1). In 10x Genomics Chromium libraries, we also found abundant discordant priming from the more commonly occurring intronic-polyT sequences (Extended Data Fig. 1), which may have been generated during PCR amplification by priming on the first-strand cDNA. The substantial number of intronic molecules and their correlation with the exonic counts suggest that these molecules represent unspliced precursor mRNAs. This was confirmed by metabolic labelling of newly transcribed RNA[9] followed by RNA sequencing using oligo-dT-primed single-cell-tagged reverse transcription (STRT)[10] (Extended Data Fig. 2); 83% of all genes displayed expression time courses consistent with simple first-order kinetics, as expected if unspliced reads represent nascent mRNA.

To quantify the time-dependent relationship between the abundance of precursor and mature mRNA, we assumed a simple model for transcriptional dynamics[2], in which the first time derivative of the spliced mRNA abundance (RNA velocity) is determined by the balance between production of spliced mRNA from unspliced mRNA, and the mRNA degradation (Fig. 1b and Supplementary Note 1). Under such a model, steady states are approached asymptotically when the rate of transcription α is constant, with the steady-state abundances of spliced (s) and unspliced (u) molecules determined by α, and constrained to a fixed-slope relationship where $u = \gamma s$ (Supplementary Note 2 Section 1). The equilibrium slope γ combines degradation and splicing rates, capturing gene-specific regulatory properties, the ratio of intronic and exonic lengths, and the number of internal priming sites. Using a recently published compendium of mouse tissues[11], we found that the steady-state behaviour of most genes across a wide range of cell types was consistent with a single fixed slope γ (Extended Data Fig. 3a–c). However, 11% of genes showed distinct slopes in different subsets of tissues (Extended Data Fig. 3d, e), suggesting tissue-specific alternative splicing (Extended Data Fig. 3f) or degradation rates.

During a dynamic process, an increase in the transcription rate α results in a rapid increase in unspliced mRNA, followed by a subsequent increase in spliced mRNA (Fig. 1c and Supplementary Note 2 Section 1) until a new steady state is reached. Conversely, a drop in the rate of transcription first leads to a rapid drop in unspliced mRNA, followed by a reduction in spliced mRNAs. During induction of gene expression, unspliced mRNAs are present in excess of the expectation based on the equilibrium rate γ, whereas the opposite is true during repression (Fig. 1d). The balance of unspliced and spliced mRNA abundance is, therefore, an indicator of the future state of mature mRNA abundance, and thus the future state of the cell.

To demonstrate how this simple model can be used to extrapolate the mature mRNA abundance into the future, we examined a time course of bulk RNA-seq measurements of the circadian cycle in the mouse liver[12]. Unspliced mRNA levels at each time point were consistently more similar to the spliced mRNA of the subsequent time (Fig. 1e), and many circadian-associated genes showed the expected excess of unspliced mRNA relative to the slope γ during upregulation, and a corresponding deficit during downregulation (Fig. 1f, g). Solving the proposed differential equations for each gene allowed us to extrapolate each measurement throughout the circadian cycle, accurately capturing the expected direction of progression of the circadian cycle (Fig. 1h).

Next, to demonstrate the ability to predict transcriptional dynamics in single-cell measurements, we analysed recently published single-cell mRNA-seq data of mouse chromaffin cells[13], obtained using SMART-seq2[5] (Fig. 2). During development, a substantial proportion of chromaffin cells, which are neuroendocrine cells of the adrenal medulla, arise from Schwann cell precursors, providing a convenient test case in which the direction of differentiation can be validated by lineage tracing. Phase portraits of many genes showed the expected deviations

[1]Laboratory of Molecular Neurobiology, Department of Medical Biochemistry and Biophysics, Karolinska Institutet, Stockholm, Sweden. [2]Science for Life Laboratory, Solna, Sweden. [3]Department of Biomedical Informatics, Harvard Medical School, Boston, MA, USA. [4]Department of Applied Mathematics, Peter The Great St. Petersburg Polytechnic University, St, Petersburg, Russia. [5]Department of Biosciences and Nutrition, Karolinska Institutet, Stockholm, Sweden. [6]Department of Physiology and Pharmacology, Karolinska Institutet, Stockholm, Sweden. [7]John van Geest Centre for Brain Repair, Department of Clinical Neurosciences, University of Cambridge, Cambridge, UK. [8]Division of Neurodegeneration, Department of Neurobiology, Care Sciences and Society, Karolinska Institutet, Stockholm, Sweden. [9]Max Planck Institute for Biophysical Chemistry, Department of Molecular Biology, Göttingen, Germany. [10]Harvard Stem Cell Institute, Cambridge, MA, USA. *e-mail: sten.linnarsson@ki.se; peter_kharchenko@hms.harvard.edu

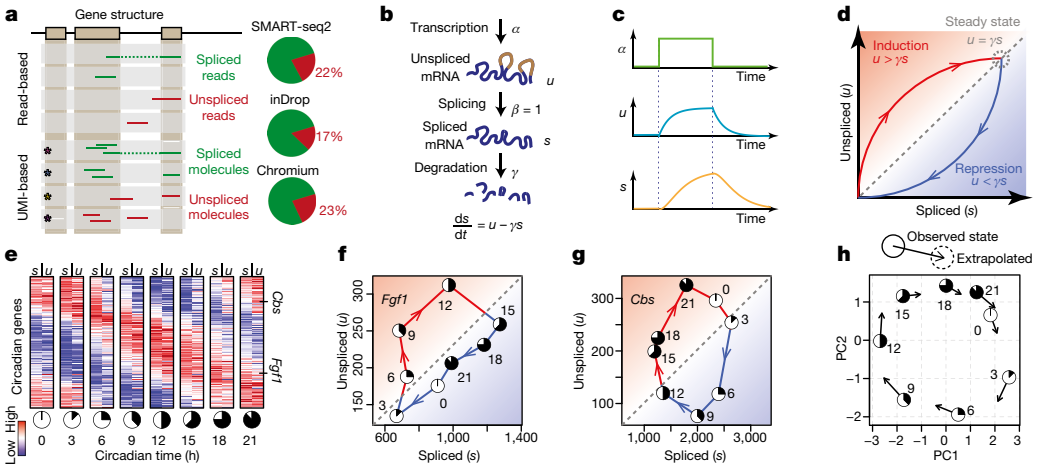

Fig. 1 | Balance between unspliced and spliced mRNAs is predictive of cellular state progression. a, Spliced and unspliced counts are estimated by separately counting reads that incorporate the intronic sequence. Multiple reads associated with a given molecule are grouped (boxes with asterisks) for unique molecular identifier (UMI)-based protocols. Pie charts show typical fractions of unspliced molecules. **b**, Model of transcriptional dynamics, capturing transcription (α), splicing (β) and degradation (γ) rates involved in production of unspliced (u) and spliced (s) mRNA products. **c**, Solution of the model in **b** as a function of time, showing unspliced and spliced mRNA dynamics in response to step changes in α. **d**, Phase portrait showing the same solution shown in **c** (solid curves). Steady states for different values of transcription rates α fall on the diagonal given by slope γ (dashed line). Levels of unspliced mRNA above or below this proportion indicate increasing (red shading) or decreasing (blue shading) expression of a gene, respectively. **e**, Abundance of spliced (s) and unspliced (u) mRNAs for circadian-associated genes in the mouse liver over a 24-h time course[12]. The unspliced mRNAs are predictive of spliced mRNA at the next time point. **f**, **g**, Phase portraits observed for a pair of circadian-driven genes: *Fgf1* (**f**) and *Cbs* (**g**). The circadian time of each point is shown using a clock symbol (corresponding to those in **e**). The dashed diagonal line shows the steady-state relationship, as predicted by γ fit. **h**, Change in expression state at a future time t, as predicted by the model, is shown in the space of the first two principal components (PCs), recapitulating the progression along the circadian cycle. Each circle shows the observed expression state, with the arrow pointing to the position of the future state, extrapolated from velocity estimates.

from the predicted steady-state relationship (Fig. 2b, c). RNA velocity estimates of the individual cells accurately recapitulated the transcriptional dynamics within this dataset, including general movement of the differentiating cells towards a chromaffin fate (Fig. 2d), as well as the movement towards and away from the intermediate differentiation state. The velocity also captured cell-cycle dynamics involved in the chromaffin differentiation, both in principle component analysis (PCA) projection and in a focused analysis of cell-cycle associated genes (Supplementary Note 2 Section 5).

Our velocity estimation procedure incorporates several features to accommodate the complexity of splicing biology (Supplementary Note 1). The estimation of the gene-specific equilibrium coefficient γ is performed using regression on the extreme expression quantiles, ensuring robust estimation even when most of the observed cells are outside of the steady state (Supplementary Note 2 Section 2). To accommodate genes observed far outside of their steady state, we also developed an alternative fit based on gene structure (Extended Data Fig. 4). A variety of techniques can be used to visualize the velocity estimates in low dimensions. The observed and extrapolated cell states can be jointly embedded in a common low-dimensional space (for example, PCA in Fig. 2d). Alternatively, velocities can be projected onto existing low-dimensional embeddings, such as t-distributed stochastic neighbour embedding (t-SNE), on the basis of the similarity of the extrapolated state to other cells in the local neighbourhood (Fig. 2h, see Supplementary Note 1). In large datasets, it is easier to visualize the prevalent pattern of cell velocities with locally averaged vector fields (Fig. 2i). Because cells can have RNA velocities along multiple independent components simultaneously, such as differentiation, maturation and proliferation, care must be taken when interpreting low-dimensional representations, as cells that lack apparent velocity in one particular embedding can nevertheless have substantial velocity in some subspace that is not visualized.

Cell-specific RNA velocity estimates provide a natural basis for quantitative modelling of cell fates. Metabolic labelling showed that for most genes, changes in the spliced/unspliced ratio would be detectable after 10–100 min (Extended Data Fig. 2). The effective timescale of extrapolation, on the other hand, depends on the biological process that is analysed. On the basis of pulse labelling of chromaffin progenitor cells with 5-ethynyl-2′-deoxyuridine (EdU) (Supplementary Note 2 Section 6), we estimate that we were able to extrapolate 2.5–3.8 h into the future (Fig. 2f, g), which is also consistent with the ability to resolve cell-cycle events. Given the linear nature of the extrapolation, however, this predictive timescale will depend on the shape of the gene expression trajectory (that is, the curvature of the expression manifold). Cell fates can be predicted over longer time scales by tracing a sequence of small extrapolation steps on the observed expression manifold (Supplementary Note 2 Section 7).

To demonstrate the generality of our approach we analysed data generated using additional single-cell RNA-seq protocols. We observed the transcriptional dynamics of neutrophil maturation in mouse bone marrow, and of light-induced neuronal activation in mouse cortex measured using the inDrop protocol (Extended Data Fig. 5), and of the intestinal epithelium (Extended Data Fig. 6), oligodendrocyte differentiation (Extended Data Fig. 7) and hippocampus development (see below), measured using 10x Genomics Chromium[7]. Estimates of RNA velocity were robust to variations in the model parameters, and gene and cell subsampling, with the most sensitive parameter being the size of the neighbourhood used in the visualization of velocity in pre-defined embeddings (Supplementary Note 2 Sections 10, 11). Most genes showed a positive correlation between velocity estimates and empirically observed expression derivatives (Extended Data Fig. 8), confirming that velocity vectors are informative. Failures in specific cases had several apparent causes, including genes observed exclusively far from equilibrium, uneven contribution of non-coding transcripts, and alternative splicing leading to multiple rates of γ across the measured populations (Supplementary Note 2 Section 4).

We next applied RNA velocity to the branching lineage of the developing mouse hippocampus[14]. After removing vascular and immune cells, and GABAergic (γ-aminobutyric-acid-releasing) and Cajal–Retzius neurons (which originate from outside the hippocampus), t-SNE plot revealed a complex manifold with multiple branches (Fig. 3a). We used known markers to identify the tips of the

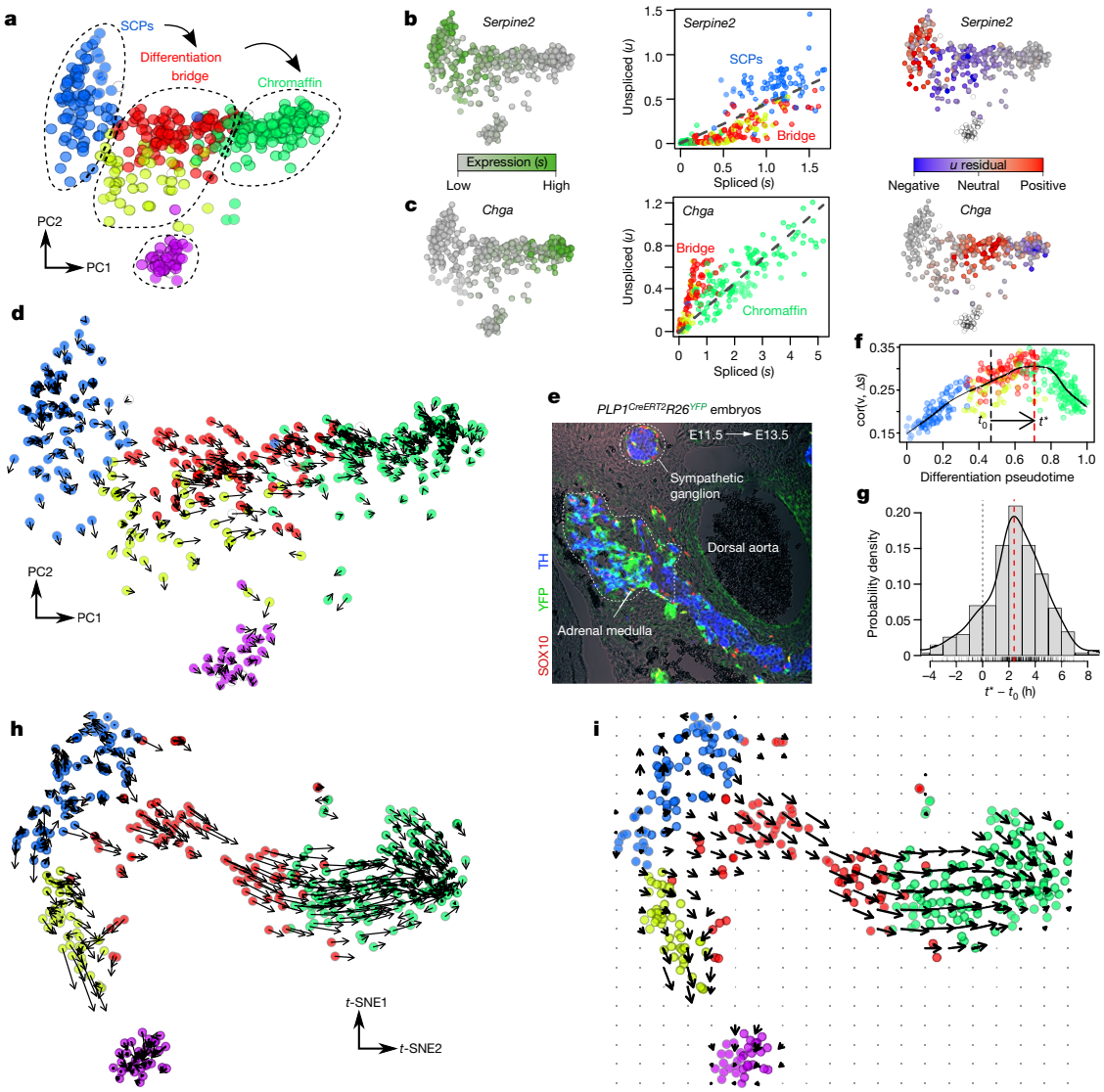

Fig. 2 | RNA velocity recapitulates dynamics of chromaffin cell differentiation. **a**, PCA projection showing major subpopulations of Schwann cell precursors (SCPs) differentiating into chromaffin cells in embryonic day (E)12.5 mice ($n = 385$ cells). **b**, **c**, Expression pattern (left), unspliced–spliced phase portraits (centre, cells coloured according to **a**), and u residuals (right) are shown for the repressed *Serpine2* (**b**) and induced *Chga* (**c**) genes. Read counts were pooled across the five nearest cell neighbours. **d**, The observed and the extrapolated future states (arrows) are shown on the first two PCs. RNA velocity was estimated without cell or gene pooling. **e**, SCP-to-chromaffin cell transition as evidenced by lineage tracing with SCP-specific PLP1-CreERT2 line. A cross-section through the developing adrenal medulla is shown. Note the high proportion of TH^+YFP^+ cells in the developing medulla and the absence of such double-positive cells in the sympathetic ganglion ($n = 3$ replicates). YFP labels $Htr3a^+$ bridge cells; TH marks chromaffin cells; TH^+YFP^+ marks chromaffin cells that are freshly differentiated from the bridge population. **f**, Extrapolation distance along the chromaffin differentiation trajectory is estimated for a single cell at pseudotime t_0, on the basis of the correlation (y axis) between the velocity v and cell expression difference. The red line shows optimal extrapolation time (t^*) (see Supplementary Note 2 Section 6). **g**, Distribution of optimal extrapolation times ($t^* - t_0$) for the chromaffin differentiation time course. The red line marks the distribution mode (2.1 h). **h**, The velocities are visualized on the pre-defined t-SNE plot from the original publication[13]. Velocity estimates based on nearest-cell pooling ($k = 5$) were used. **i**, Same velocity field as **h**, visualized using Gaussian smoothing on a regular grid.

branches that corresponded to astrocytes, oligodendrocyte precursors (OPCs), dentate gyrus granule neurons and pyramidal neurons of the five fields of the hippocampus: the subiculum, CA1, CA2, CA3 and hilus (Extended Data Fig. 9). Phase portraits of individual genes showed specific induction and repression of gene expression along the manifold (Fig. 3b and Extended Data Fig. 10). For example, *Pdgfra* (a marker of OPCs) was induced in pre-OPCs and maintained in OPCs; it showed corresponding positive velocity in the pre-OPC state, but was neutral in the OPCs. Similarly, *Igfbpl1* was expressed specifically in neuroblasts and showed positive velocity from radial glia to neuroblasts, but negative velocity going from neuroblasts to the two main neuronal branches.

RNA velocity showed a strong directional flow towards each of the main branches (Fig. 3c and Extended Data Fig. 10), originating in a small group of cells arranged in a band (Fig. 3c, inset, dashed line). We identified these cells as radial glia on the basis of the expression of markers, including the Notch target *Hes1* and the homeobox transcription factor *Hopx* (Extended Data Fig. 9). Indeed, fate mapping has previously shown radial glia to be the true origin of the lineage tree of the hippocampus[15]. Using a Markov random-walk model on the velocity field, the terminal and root states could be automatically identified (Fig. 3c), demonstrating the power of RNA velocity to orient the lineage tree without prior knowledge about the developmental process. On one side, velocity pointed towards astrocytes (expressing *Aqp4*) without

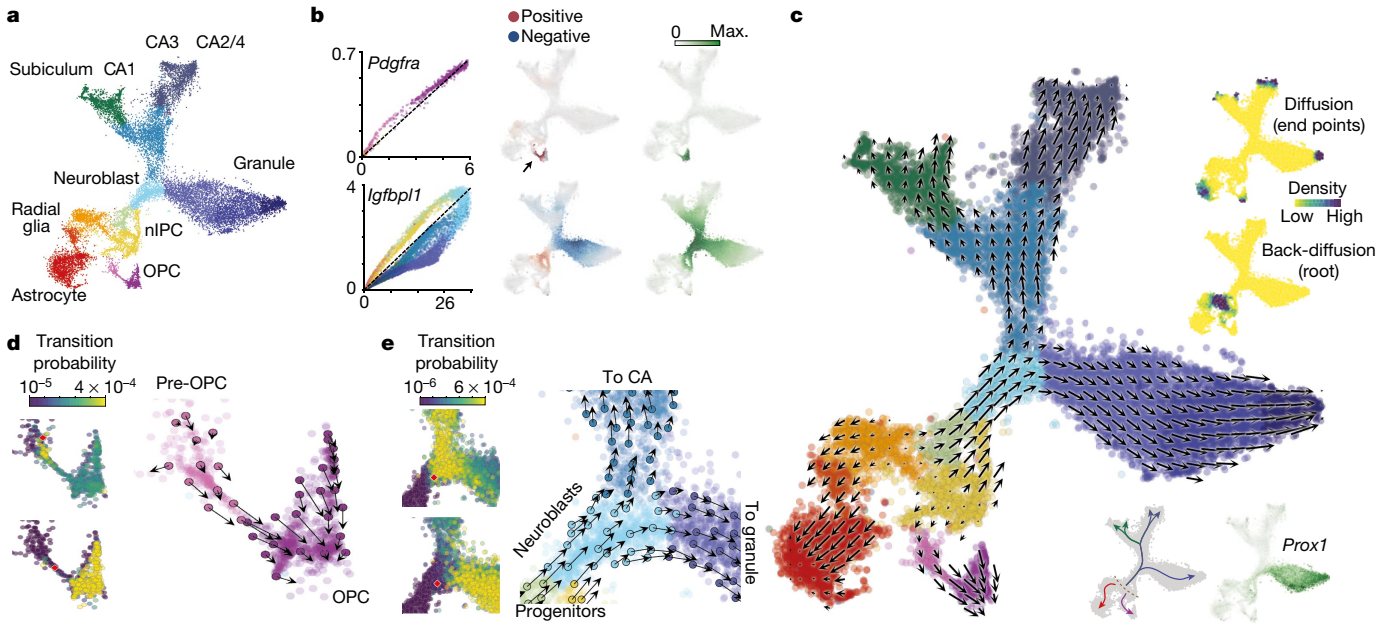

Fig. 3 | RNA velocity field describes fate decisions of major neural lineages in the hippocampus. a, *t*-SNE plot of the developing mouse hippocampus cells ($n = 18{,}213$ cells), showing major transient and mature subpopulations. **b**, Phase portraits (left, coloured as in **a**), unspliced residuals (middle) and spliced expression (right) are shown for two regulated genes. *k*-nearest neighbour (*k*NN) cell pooling was used. **c**, Velocity field projected onto the *t*-SNE plot. Arrows show the local average velocity evaluated on a regular grid. Top right inset, differentiation endpoints as high density regions on the manifold after forward Markov process with velocity-based transition probabilities; the root of the branching tree is identified simulating the process in the reverse direction. Bottom right inset, summary schematic of the RNA velocity field, and expression of the transcription factor *Prox1*. **d**, Commitment to oligodendrocyte fate. Left, visualization of single-step transition probabilities from two starting cells (red) to neighbouring cells. Right, velocities of a sampled subset of cells shown on the *t*-SNE plot in **c**. **e**, Fate decision of neuroblasts. Left, visualization of single-step transition probabilities from two starting cells (red) to neighbouring cells. Right, velocities of a sampled subset of cells shown on the *t*-SNE plot in **c**.

intervening cell division, or alternatively to a pre-OPC state, leading through a narrow passage to proliferating OPCs. We speculated that the narrow passage represented the moment of commitment to the oligodendrocyte lineage. At this microstate level, fate choice is likely to be a non-deterministic process involving the tilting of gene expression in favour of one or the other fate, followed by a lock-in of the final fate once transcription-factor feedback loops are established[16]. Comparing the probability distribution of future states for a cell starting among the pre-OPCs, with one starting in the narrow passage leading to OPCs revealed a clear difference—the latter cell was overwhelmingly likely to end up as a fully formed OPC whereas the former was as likely to remain in the pre-OPC state (Fig. 3d).

Some cycling progenitor cells (Extended Data Fig. 9b) expressed neurogenic transcription factors (for example, *Neurod2*, *Neurod4*, *Eomes*), and those cells showed velocity towards the immature neuroblast state, leading towards the three main neuronal branches in the upper part of the manifold. Granule neurons of the dentate gyrus first split from the hippocampus proper, and a second split divided the hippocampal cells into subiculum/CA1 and CA2–4, respectively (Extended Data Figs. 9, 10), in agreement with the major functional and anatomical subdivisions of the hippocampus. The detailed, single-cell view of a branching lineage allowed us to interrogate fate choice. Examining two adjacent neuroblasts just at the entrance to the branching point between CA and granule fates (Fig. 3e), we found that although their current states were neighbours (in gene-expression space), their futures were already tilted towards different fates, distinguished by activation of *Prox1* (Fig. 3c, inset). Consistent with these findings, it has been shown that *Prox1* is required for the formation of granule neurons and that, when *Prox1* is deleted, neuroblasts instead adopt a pyramidal neuron fate[17].

To demonstrate that RNA velocity is detectable in the human embryo, we performed droplet-based single-cell mRNA-seq of the developing human forebrain at ten weeks post-conception, focusing on the glutamatergic neuronal lineage (Fig. 4a). We found a strong velocity pattern originating from a proliferating progenitor state (radial glia), and proceeding through a sequence of intermediate neuroblast stages to a more mature differentiated glutamatergic neuron expressing *SLC17A7* (the vesicular glutamate transporter (which is also known as *VGLUT1*) used in forebrain excitatory neurons). We validated the expression of known and novel markers of cortical neuron development by multiplexed in situ hybridization (Fig. 4b, c), confirming the predicted expression of *CLU* and *FBXO32* in the ventricular zone (radial glia; marked by *SOX2*), *UNC5D* in the intermediate zone (neuroblasts; marked by *EOMES*) and *SEZ6* and *RBFOX1* in the cortical plate (neurons; marked by *SLC17A7*). The layered expression of these genes in the tissue (Fig. 4c) corresponded closely to the pseudotemporal distribution of their expression in the single-cell RNA-seq data (Fig. 4b).

We used principal curve analysis to order the cells according to a differentiation pseudotime, and examined the temporal progression of transcription in human primary cells. We confirmed that unspliced mRNAs consistently preceded spliced mRNAs during both up- and downregulation (Fig. 4d). We observed both fast and slow kinetics. For example, *RNASEH2B* exhibited fast kinetics, with little difference between unspliced and spliced RNAs. By contrast, genes such as *DCX*, *ELAVL4* and *STMN2* showed evidence of an initial burst of rapid transcription, followed by sustained transcription at a reduced level (as evidenced by the shape of the unspliced RNA curve, Fig. 4d), with spliced transcripts following a noticeably delayed trajectory. Such dynamic induction with overshooting has been proposed to help to quickly induce genes with slow degradation kinetics[2], but this has not been possible to study in human embryos.

As RNA velocity is grounded in real transcription kinetics, this approach promises to bring a more solid quantitative foundation to our understanding of the dynamics of cells in gene-expression space during differentiation. We envision future manifold learning algorithms that simultaneously fit a manifold and the kinetics on that manifold, on the basis of RNA velocity. RNA velocity has already enabled the detailed

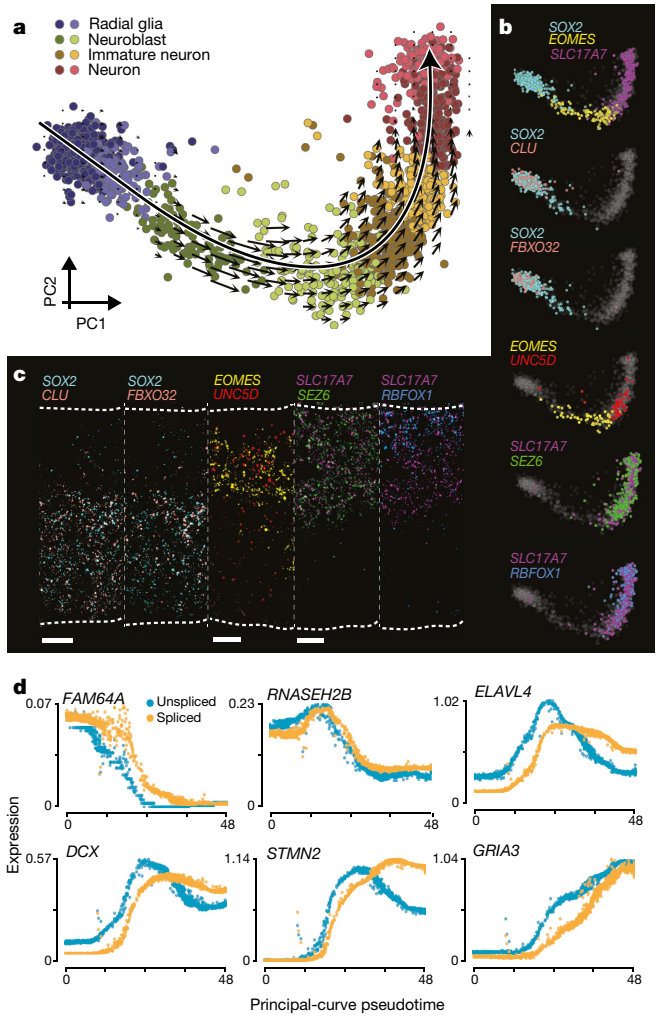

Fig. 4 | Kinetics of transcription during human embryonic glutamatergic neurogenesis. a, PCA projection of human glutamatergic neuron differentiation ($n = 1{,}720$ cells) at post-conception week 10, shown with velocity field. Colours indicate cell types and intermediate states. A corresponding principal curve is shown in bold. **b**, Gene expression of known markers of radial glia (*SOX2*), neuroblasts (*EOMES*) and neurons (*SLC17A7*), and of novel markers is visualized on the PCA projection for the indicated genes in pseudocolour. **c**, Fluorescent in situ hybridization (RNAscope) for the same genes as in **b** on a cross-section of human developing cortex, oriented with the ventricular zone towards the bottom and the cortical surface towards the top ($n = 1$). Scale bars, 25 μm. **d**, Pseudotime expression profiles during glutamatergic neuron maturation for six example genes. Spliced abundance was multiplied by γ to match the scale of unspliced abundance.

study of dynamic processes in whole organisms[18], and will greatly facilitate lineage analysis particularly in the human embryo.

Online content

Any Methods, including any statements of data availability and Nature Research reporting summaries, along with any additional references and Source Data files, are available in the online version of the paper at https://doi.org/10.1038/s41586-018-0414-6.

Received: 13 December 2017; Accepted: 3 July 2018;
Published online: 08 August 2018

1. Linnarsson, S. & Teichmann, S. A. Single-cell genomics: coming of age. *Genome Biol.* **17**, 97 (2016).
2. Zeisel, A. et al. Coupled pre-mRNA and mRNA dynamics unveil operational strategies underlying transcriptional responses to stimuli. *Mol. Syst. Biol.* **7**, 529 (2011).
3. Gray, J. M. et al. SnapShot-Seq: a method for extracting genome-wide, in vivo mRNA dynamics from a single total RNA sample. *PLoS ONE* **9**, e89673 (2014).
4. Gaidatzis, D., Burger, L., Florescu, M. & Stadler, M. B. Analysis of intronic and exonic reads in RNA-seq data characterizes transcriptional and post-transcriptional regulation. *Nat. Biotechnol.* **33**, 722–729 (2015).
5. Picelli, S. et al. Smart-seq2 for sensitive full-length transcriptome profiling in single cells. *Nat. Methods* **10**, 1096–1098 (2013).
6. Islam, S. et al. Quantitative single-cell RNA-seq with unique molecular identifiers. *Nat. Methods* **11**, 163–166 (2013).
7. Klein, A. M. M. et al. Droplet barcoding for single-cell transcriptomics applied to embryonic stem cells. *Cell* **161**, 1187–1201 (2015).
8. Zheng, G. X. Y. et al. Massively parallel digital transcriptional profiling of single cells. *Nat. Commun.* **8**, 14049 (2017).
9. Schwalb, B. et al. TT-seq maps the human transient transcriptome. *Science* **352**, 1225–1228 (2017).
10. Islam, S. et al. Characterization of the single-cell transcriptional landscape by highly multiplex RNA-seq. *Genome Res.* **21**, 1160–1167 (2011).
11. The Tabula Muris Consortium, Quake, S. R., Wyss-Coray, T., & Darmanis, S. Single-cell transcriptomic characterization of 20 organs and tissues from individual mice creates a Tabula Muris. Preprint at https://biorxiv.org/content/early/2018/03/29/237446 (2018).
12. Vollmers, C. et al. Circadian oscillations of protein-coding and regulatory RNAs in a highly dynamic mammalian liver epigenome. *Cell Metab.* **16**, 833–845 (2012).
13. Furlan, A. et al. Multipotent peripheral glial cells generate neuroendocrine cells of the adrenal medulla. *Science* **357**, eaal3753 (2017).
14. Kriegstein, A. & Alvarez-Buylla, A. The glial nature of embryonic and adult neural stem cells. *Annu. Rev. Neurosci.* **32**, 149–184 (2009).
15. Malatesta, P. et al. Neuronal or glial progeny: regional differences in radial glia fate. *Neuron* **37**, 751–764 (2003).
16. Johnston, R. J. & Desplan, C. Stochastic mechanisms of cell fate specification that yield random or robust outcomes. *Annu. Rev. Cell Dev. Biol.* **26**, 689–719 (2010).
17. Iwano, T., Masuda, A., Kiyonari, H., Enomoto, H. & Matsuzaki, F. Prox1 postmitotically defines dentate gyrus cells by specifying granule cell identity over CA3 pyramidal cell fate in the hippocampus. *Development* **139**, 3051–3062 (2012).
18. Plass, M. et al. Prox1 postmitotically defines dentate gyrus cells by specifying granule cell identity over CA3 pyramidal cell fate in the hippocampus. *Science* **360**, eaaq1723 (2018).

Acknowledgements The work reported here was supported by the Swedish Foundation for Strategic Research (RIF14-0057 and SB16-0065), the Knut and Alice Wallenberg Foundation (2015.0041), the Erling Persson Foundation (HumDevCellAtlas) and the Wellcome Trust (108726/Z/15/Z) to S.L.; Center for Innovative Medicine (CIMED) to K.L. and P.C.; Swedish Research Council, Marie Curie Integration Grant EPIOPC, 333713, European Research Council EPIScOPE, 681893, Swedish Brain Foundation, Ming Wai Lau Centre for Reparative Medicine, Cancerfonden and Karolinska Institutet to G.C.-B. P.V.K. was supported by NIH R01HL131768 from NHLBI and CAREER (NSF-14-532) award from NSF.

Reviewer information *Nature* thanks A. Klein, R. Satija, M. Stadler and the other anonymous reviewer(s) for their contribution to the peer review of this work.

Author contributions S.L. conceived the concept of RNA velocity and P.V.K. showed that RNA velocity could be detected through analysis of unspliced transcripts in single cells. P.V.K. and S.L. designed and supervised the study. P.V.K., S.L., G.L.M. and R.S. developed the analytical framework, analysed data, made figures and drafted the manuscript, with contributions from all co-authors. P.V.K., G.L.M., R.S. and P.L. implemented the software, with assistance from V.P. and J.F. Z.L. examined RNA degradation signals. A.Z. and H.H. performed the mouse hippocampus experiment. P.C. supervised and K.L. and H.H. performed metabolic labelling. M.E.K. and I.A. performed validations of chromaffin differentiation rate. E.B. and L.E.B. performed and analysed the fluorescent in situ hybridization experiment on tissue dissected by X.H. E.S. and R.B. provided human embryonic brain tissue. D.v.B. performed the human forebrain single-cell RNA-seq experiment under supervision of G.C.-B. J.G. assisted with measurement and interpretation of mouse bone marrow. The paper was read and approved by all co-authors.

Competing interests The authors declare no competing interests.

Additional information
Extended data is available for this paper at https://doi.org/10.1038/s41586-018-0414-6.
Supplementary information is available for this paper at https://doi.org/10.1038/s41586-018-0414-6.
Reprints and permissions information is available at http://www.nature.com/reprints.
Correspondence and requests for materials should be addressed to S.L. and P.V.K.
Publisher's note: Springer Nature remains neutral with regard to jurisdictional claims in published maps and institutional affiliations.

METHODS

No statistical methods were used to predetermine sample size. The experiments were not randomized. The investigators were not blinded to allocation during experiments and outcome assessment.

Theoretical description of RNA velocity. On the basis of the model of transcription shown in Fig. 1, we developed a computational framework for robust inference of RNA velocity. A detailed description of the theory and computational methods is available as Supplementary Note 1.

Analysis pipeline, parameters and implementations. We implemented the procedures above as two complete pipelines, one in R and one in Python, called velocyto.R and velocyto.py, respectively. These were used to generate all of the analyses in the paper, with detailed settings as described in the following sections.

Annotation of spliced and unspliced reads. Read annotation for all protocols was performed using velocyto.py command-line tools. The velocyto.py annotation starts with BAM file(s). For the 10x genomics platform datasets, the BAM file was processed using the default parameters of the Cellranger software (10x Genomics). For the inDrop dataset, the reads were demultiplexed using dropEst pipeline[19], using '-F -L eiEIBA' options to produce an annotated BAM file analogous to Cellranger output. For SMART-seq2 data, demultiplexed cell-specific BAM files were fed into velocyto.py directly. The genome annotations GRCm38.84 and GRCh37.82 from the Cellranger pre-built packages were used to count molecules while separating them into three categories: 'spliced', 'unspliced' or 'ambiguous'.

The annotation process considered only reads that could be mapped uniquely. Reads with multiple mappings and reads mapped inside repeat-masked (based on the UCSC genome browser repeat masker output) regions were discarded. For UMI-based protocols, the counting was performed at the level of molecules, taking the annotation (such as spliced, unspliced, etc.) of all reads associated with that molecule (supporting read sets) into consideration. The supporting read sets for each molecule were determined by a combination of cell barcode and UMI sequence. For inDrops datasets, where UMI barcode does not have sufficient complexity to uniquely identify a molecule in the dataset, the reads were grouped based on the cell barcode, UMI and the region of the genome where it mapped (chromosomes, binned in 10-Mb regions). For each molecule, all annotated transcripts that were compatible with the given set of read mappings were considered, and cases where the set of reads associated with a given molecule was not compatible with any annotated transcript model were discarded. Cases where a set of supporting read mappings was compatible with transcript models of two or more different genes were also discarded.

The following set of rules was applied to annotate a set of reads supporting a given molecule as spliced, unspliced or ambiguous:

1. A molecule was annotated as spliced if all of the reads in the set supporting a given molecule map only to the exonic regions of the compatible transcripts.
2. A molecule was annotated as unspliced if all of the compatible transcript models had at least one read among the supporting set of reads for this molecule mapping that (i) spanned exon-intron boundary, or (ii) mapped to the intron of that transcript.

Molecules for which some of the compatible transcript models had exonic-only mappings, while others included intronic mappings, were annotated as ambiguous and not used in the downstream analyses.

A similar logic was applied when annotating and counting reads for the SMART-seq2 dataset, with the following notable differences: (1) as reads lacked UMIs, each read was considered to be an independent molecule; (2) as the protocol does not distinguish strands, transcript annotations on both strands were considered when annotating each read.

Chromaffin dataset processing. Data analysis for Fig. 2. Chromaffin datasets of mice aged embryonic day (E)12.5 and E13.5 were processed using the velocyto.R pipeline. The γ coefficients and velocity estimates were calculated for genes meeting a number of filtering criteria: $\gamma \geq 0.1$; Spearman rank correlation between s and $u \geq 1$; average s counts for a gene ≥ 5 for at least one cell subpopulation (cluster); average u counts for a gene ≥ 1 for at least one cell subpopulation; for the datasets where spanning reads were annotated (E12.5, E13.5), average spanning read counts were required to be ≥ 5 in at least one subpopulation. For SMART-seq2 datasets, the abundance of reads spanning intron and exon boundaries is sufficiently high to enable estimation of the unspliced offset o. The offset was estimated using linear regression.

Mouse hippocampus dataset analysis. Data analysis for Fig. 3. A total of 18,213 cells were analysed (postnatal day (P)0: 8,113 cells; postnatal day (P)5: 10,100 cells). The embedding was computed on the correlation similarity matrix using pagoda2 (https://github.com/hms-dbmi/pagoda2). In brief, gene variance normalization was performed by fitting a generalized additive model of variance on expression magnitude, and rescaling the gene variance by matching the tail probabilities of log residuals from the F distribution to the χ^2 distribution with the degrees of freedom corresponding to the total number of cells. Cell distances were determined as $1 - r_{ij}$,where r_{ij} is Pearson linear correlation of the cell i and j scores on the first 100 principal components of the top 3,000 variable genes in the dataset. Clustering was performed using the Louvain community detection algorithm on the nearest neighbour cell graph ($k = 30$, pagoda2 implementation). For the velocity analysis lowly expressed (spliced) genes were excluded (requiring 40 minimum expressed counts and detected over 30 cells) and the top 3,000 high variable genes were selected on the basis of a non-parametric fit of the coefficient of variation (CV) using the mean as predictor (using support vector regression). Only 1,706 genes that had unspliced molecule counts above a detection threshold (25 minimum expressed counts and detected over 20 cells) were kept for the analysis. To normalize for the cell size, the counts were divided by the total number of molecules in each cell, and multiplied by the mean number of molecules across all cells. Spliced and unspliced counts were normalized separately. To reduce dimensionality, PCA was performed and the top 19 variable components were kept on the basis of the explained variance ratio profile. Euclidean distance in this reduced PCA space was used to construct a kNN graph ($k = 500$), using a greedy balanced kNN algorithm that limits each node to a maximum of $4k$ incoming edges. This graph was used to perform kNN pooling. Velocity-based extrapolation was performed using model I assumptions.

Human glutamatergic neurogenesis analysis. Data analysis for Fig. 4. Pseudotime analysis was performed by fitting principal curve in the space of the top four principal components (using the R package princurve). The cell positions were projected onto the curve and the length of the arc between projections was used as pseudotime coordinates. The direction of the pseudotime was determined using the velocity field. Clusters were determined using Louvain community detection algorithm on the nearest neighbour graph in the same subspace. For the velocity analysis lowly expressed (spliced) genes were excluded (requiring 30 minimum expressed counts and detected over 20 cells). The top 2,000 most variable genes were selected on the basis of a non-parametric fit of CV versus mean (using support vector regression). A total of 987 genes that had unspliced molecules above a detection threshold (requiring 25 minimum expressed counts and detected over 20 cells; average spliced counts for a gene 0.06 in a subpopulation and average unspliced counts for a gene 0.007 in a subpopulation) were kept for the analysis. To normalize for the cell size, the counts were divided by the total number of molecules in each cell and multiplied by the median number of molecules across all cells. For cell kNN pooling, a k-nearest neighbour graph ($k = 550$) was constructed based on Euclidean distance in the space of the top six principal components, as described above. The γ coefficients were fit using the extreme quantile fit with diagonal quantiles, as described above.

For the visualizations in Fig. 4b, the following maximum-projection procedure was used to colour the cells according to expression of the pre-defined gene set. First, the (cell-size normalized) expression of each gene included in the set was rescaled, dividing it by the 98th percentile magnitude. After rescaling, each cell was coloured with the colour corresponding to the gene that was expressed at highest level compared to other genes, and the saturation of the colour was chosen to be proportional to the level of expression in the cell. The rescaled expression of the gene was required to exceed 0.45 in order for the cell to be coloured.

Genes whose expression peaks at different stages of neurogenesis were selected using a heuristic gene enrichment score: where μ indicates the average molecule count of a gene and f is the fraction of cells in which the gene is detected. Figure 4d shows a selection of top-enriched genes, spliced and unspliced molecules were brought to a comparable scale by multiplying spliced molecular counts by the estimated γ.

Analysis of mouse oligodendrocytes lineage. Data analysis for Extended Data Fig. 7. We analysed a dataset of oligodendrocyte differentiation from mouse pons extracted from a recently published cellular atlas[20]. We restricted the analysis to the trajectory of differentiation from OPCs to mature oligodendrocytes by selecting cells that were labelled in the atlas as OPCs, committed oligodendrocyte precursor cells, newly formed oligodendrocytes and myelin-forming oligodendrocytes, for a total of 6,307 cells.

As an initial step, for Extended Data Fig. 7d–f, we performed a straightforward feature selection, first removing genes for which fewer than 15 spliced molecules were expressed, or fewer than 8 unspliced molecules, requiring a minimal average spliced expression of 0.075 and minimal unspliced expression of 0.03 in the highest expressing cluster. A CV-mean fit was used to select the 606 most variable genes.

As the simple procedure above retained significant sex-driven batch effect (shown in Extended Data Fig. 7e), we then used a different approach aimed at minimizing batch effects by focusing on the genes that were uniquely relevant to the observed oligeodendrocytes. Specifically, a list of genes enriched in the oligodendrocyte lineage when compared to all other cell types was used to analyse the dataset. For each cell cluster we used the top 190 genes as sorted by enrichment (differential upregulation) scores, calculated as described[20]. The resulting set of genes was subjected to further filtering where lowly detected genes were excluded, requiring at least 5 spliced and 3 unspliced mRNA molecules detected in the whole dataset, resulting in 606 genes. We then normalized the cell total molecule counts using the initial molecule count as a normalization factor. For cell kNN pooling we built a k-nearest neighbour graph ($k = 90$) based on Euclidean distance in the top nine principal components. Data were clustered using a Louvain community

detection algorithm on the nearest neighbour graph and coloured according to a pseudotime computed by a principal curve. Finally, we calculated gammas, velocity and extrapolation as described above; transition probabilities were computed using n_sight = 300 and log transform.

Analysis of visual cortex response to light simulation. Data analysis for Extended Data Fig. 5. For the pre-processing of the inDrops light-stimulated mouse visual cortex dataset[21] we used the dropEst pipeline (https://github.com/hms-dbmi/dropEst). First the droptag command was run on each FASTQ file using 10 as the minimum quality parameter. Then, mapping was performed using the STAR aligner. Finally, the dropEst command was run to perform UMI and cell barcode correction, and the following flags were passed '–m -V –b –L eiEIBA' to produce a Cellranger-like BAM file. The velocyto.py 'run_dropest' command was used to annotate and count molecules.

Cell annotations from the original publication[21] were used to extract ExcL23_1 (the largest and most homogeneous cell population described as responsive to stimulus in the original publication). We excluded cells whose total spliced RNA abundance was below the 15th percentile (as low-quality cells) and above the 99.5th percentile (as possible doublets). The dataset was further balanced by equalizing the number of cells representing each stimulation condition (unstimulated, 1-h stimulation, 4-h stimulation), randomly down-sampling subpopulations to match the number of cells in the less abundant condition. Genes whose total spliced molecule count was less than 250, or the number of expressing cells was less than 150 were removed. Similarly, we removed genes whose total unspliced molecule count was less than 18, or the number of expressing cells was less than 15. To focus our analysis on the stimulation process and to avoid capturing orthogonal variation, we performed a model-based feature selection. In brief, we considered a negative binomial generalized linear model with predictors: size (as estimated by the total number of molecules), the stimulation time (categorical and interaction with size) and no offset (that is, correspondent to the R formula: expression $\approx$ size + size:stimulation − 1). We then performed a likelihood ratio test comparing our model against the alternative model that does not take the stimulation predictor into account. Only statistically significant genes ($P < 0.001$ for spliced and $P < 0.03$ for unspliced molecules) were considered for downstream analysis. After this step, we further eliminated the cells ranking in bottom 10% of total molecular counts over all of the selected genes. For the cell *k*NN pooling, we built a *k*-nearest neighbour graph ($k = 70$) based on the Euclidean distance. Importantly, in this case, we reasoned that it was not correct to average across different independent stimulation conditions (for example, non-stimulated and 1-h stimulation), therefore pooling was only allowed between cells of the same stimulation condition. Model 2 was used for velocity-based extrapolation, with *t* set to 15. For the transition probability calculation, the n_sight parameter was set to 200, and square root was used as a variance stabilizing transformation. Early and late response genes illustrated in Extended Data Fig. 6 were extracted from the supplementary table 3 of the original publication, containing a list of significantly induced genes in different cell types[21].

Analysis of gammas over different cell types using Tabula Muris. Data analysis for Extended Data Fig. 3. The Tabula Muris dataset (including only the samples generated using droplet-based 10x Genomics Chromium protocol) was analysed using velocyto.py, using the BAM files and the valid barcodes list provided by the authors[11]. All of the experiments were merged into a single dataset. The average of spliced and unspliced raw molecule counts over the different annotated cell types were calculated, and Pearson's correlation coefficient was computed. To reduce bias associated with variation in cell coverage, we removed from the analysis the clusters with less than 120 cells as well as several outlier clusters that had more than 3,000 cells. Erythrocytes were also excluded, as they lack nuclei. To avoid inflating our correlations with trivial cases where a gene is expressed by just one or two cell types we applied the following filters: a gene was taken into consideration only if its expression levels met all of the following conditions: (1) at least 5 cell types with an average of at least 0.04 spliced molecules; (2) at least 4 cell types with an average of at least 0.02 unspliced molecules; (3) the highest expressing cell type expressed the gene at an average of at least 0.15 spliced molecules; (4) at least 2 other cell types express the gene at least 15% the level of the maximum expressing cell type. Furthermore, to avoid the inflation of correlation estimates by zeros, the correlation of each gene was calculated considering only the cell types that expressed the gene at minimum 10^{-5} spliced and 5×10^{-6} unspliced levels. The estimates of gammas provided in Extended Data Fig. 3 were obtained as the slope of RANSAC regression without intercept. Double gammas were estimated using a mixture of generalized linear regression models fitted by expectation maximization, as implemented in the R package flexmix. The fraction of genes that are better explained by two or more values of gammas than by a single gamma was estimated by comparing the double gamma model fit with a single-gamma generalized linear model fit. Specifically, a log-likelihood ratio test was used with the difference in degrees of freedom between the single- and double-gamma models taken to be the number of cell types + 1. Bonferroni correction was applied, and genes with $P < 0.05$ were reported as being significantly better explained by two gammas.

Analysis of the intestinal epithelium. Data analysis for Extended Data Fig. 6. velocyto.py was run on the BAM files and the valid barcode list provided by the authors. Cells with low levels of spliced (<2,000 molecules) and unspliced (<300 molecules) genes were filtered out. Cell cycle genes, as defined by gene ontology annotation (using Goatools) were removed from the analysis. Genes with at least 30 spliced molecules and 20 unspliced molecules in the dataset were used in the downstream analysis. No clustering was performed, instead, the cell type annotation from the original publication[22] was used. Feature selection was performed using these clusters. Specifically, the top 110 differentially upregulated genes in each cluster were selected. Genes for which minimum average expression in the highest expressing cluster was low were removed (unspliced <0.008, and spliced <0.08). PCA was performed on the cell-size-normalized data, and the first nine principal components were retained and used to calculate the *t*-SNE plot (cytograph implementation, Euclidean distance). We calculated cell *k*NN pooling using the 70 nearest neighbours, as determined by the Euclidean distance in the same nine dimensional PCA space. Gammas were fitted, velocities computed using default parameters, and extrapolation carried on using model II with $t = 4$. Transition probability was computed using n_sight of 30, using square root variance stabilizing transformation.

Human tissue and single-cell RNA sequencing. Data analysis for Fig. 4. Human first trimester forebrain tissue was obtained from elective routine abortions (10 weeks post-conception) with the written informed consent of the pregnant woman and in accordance with the ethical permit given by the Regional Ethics Vetting Board (Stockholm, Sweden, reference no. 2007/1477-31/3; for scRNA-seq), as well as from Addenbrooke's Hospital, Cambridge, UK with approval by the National Research Ethics Service Committee East of England - Cambridge Central (Local Research Ethics Committee, reference no. 96/085; for in situ hybridizations). Human fetal forebrain tissue was collected and stored in hibernation media with the addition of GlutaMAX and B-27 supplements according to the manufacturer's instructions (overnight, 4 °C, Hibernate-A, Thermo-Fisher). The tissue was then cut into small cubic pieces of approximately 1–2 mm length. Tissue was dissociated using a dissociation kit (Miltenyi, Neural Tissue Dissociation Kit (P)) according to the manufacturer's instructions. In brief, tissue was prepared in the kit buffer containing 0.067 mM β-mercaptoethanol. After addition of enzyme mix 1 and 2, the tissue was mechanically dissociated using three increasingly smaller gauges of fire-polished Pasteur pipettes, pipetted 20, 15 and 10 times up and down, respectively. Finally, collected cells were stored on ice in PBS containing 1% BSA and immediately prepared for single-cell library preparation. Single-cell RNA sequencing was performed using the 10x Genomics Chromium V2 kit, following the manufacturer's protocol, and sequenced on an Illumina Hiseq 2500.

Ethical compliance for animal experiments. All experimental procedures followed the guidelines and recommendations of Swedish animal protection legislation and were approved by the local ethical committee for experiments on laboratory animals (N68/14, Stockholms Norra Djurförsöksetiska nämnd, Sweden).

Reporting summary. Further information on experimental design is available in the Nature Research Reporting Summary linked to this paper.

Code availability. The software described in this paper, in the form of a pipeline called Velocyto (from velox, quick and κύτος, cell) is available at http://velocyto.org. This includes complete analysis libraries in R and Python, as well as R and Python notebooks.

Data availability. The data from mouse P0 and P5 hippocampus was extracted from dataset C[23], available from the Gene Expression Omnibus (GEO) under accession GSE104323. The oligodendrocyte differentiation dataset was obtained from a recent survey of the mouse nervous system[20] (Sequence Read Archive (SRA) accession SRP135960). The bulk mouse liver circadian variation RNA-seq data[12] is available at SRA accession SRA025656. The SMART-seq2 data on chromaffin cell differentiation[13] is available at GEO accession GSE99933. The mouse bone marrow dataset[19] is available at GEO accession GSE109989. The visual cortex inDrop dataset[21] is available at GEO accession GSE102827. The intestinal epithelium dataset[22] is available at GEO accession GSE92332. We have deposited the human week 10 fetal forebrain dataset in the SRA under accession code SRP129388 and the metabolic labelling data in the GEO under accession code GSE115813. All other data are available from the corresponding authors upon reasonable request.

19. Petukhov, V. et al. dropEst: pipeline for accurate estimation of molecular counts in droplet-based single-cell RNA-seq experiments. *Genome Biol.* **19**, 78 (2018).
20. Zeisel, A. et al. Molecular architecture of the mouse nervous system. Preprint at https://biorxiv.org/content/early/2018/04/06/294918 (2018).
21. Hrvatin, S. et al. Single-cell analysis of experience-dependent transcriptomic states in the mouse visual cortex. *Nat. Neurosci.* **21**, 120–129 (2018).
22. Haber, A. L. et al. A single-cell survey of the small intestinal epithelium. *Nature* **551**, 333–339 (2017).
23. Hochgerner, H., Zeisel, A., Lönnerberg, P. & Linnarsson, S. Conserved properties of dentate gyrus neurogenesis across postnatal development revealed by single-cell RNA sequencing. *Nat. Neurosci.* **21**, 290–299 (2018).
24. Lein, E. S. et al. Genome-wide atlas of gene expression in the adult mouse brain. *Nature* **445**, 168–176 (2007).

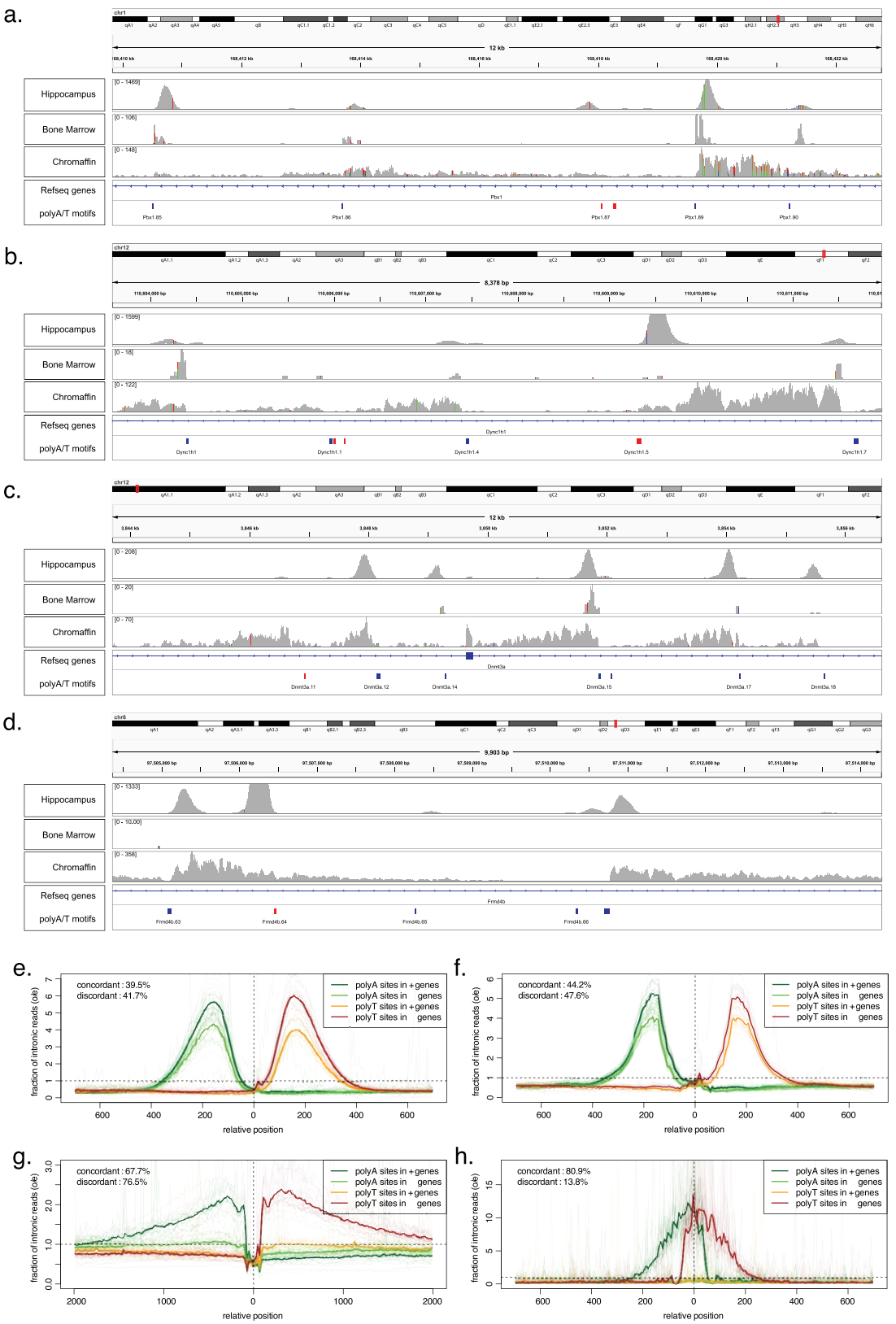

Extended Data Fig. 1 | See next page for caption.

Extended Data Fig. 1 | Most of the intronic reads arise due to internal priming from stable positions. a–d, Examples of read density around intronic polyA and polyT sequences. The browser screenshots show the density of reads from the 10x Chromium mouse hippocampus dataset (top track of each panel), mouse bone marrow inDrop dataset (second track from the top), and chromaffin differentiation assessed using SMART-seq2 (third track). The bottom two tracks show gene annotation, and positions of polyA or polyT sequences with a length of at least 15 bp with one allowed mismatch. The polyA/polyT boxes are coloured blue if the stretch is in a concordant orientation to the transcription of the underlying gene (that is, would result in a polyA sequence in the nascent RNA molecule being transcribed), or red if they are oriented in the discordant position (that is, would result in a polyT sequence in the RNA). The 3′-end-based 10x Chromium and inDrop protocols show discrete peaks downstream of the polyA priming sites, with the 10x dataset also showing peaks upstream of the polyT sites. The SMART-seq2 protocol shows much more diffused peaks, expected from the full-length purification procedure used by the protocol. **e–h**, Average read density profiles around concordant and discordant internal priming sites. The plots show observed/expected intronic read density around $(A)_{15}$ or $(T)_{15}$ sequences (with 1 allowed mismatch) within the intronic regions. The *x* axis shows position relative to the motif position (in basepairs), in a genomic reference orientation. The bold lines show genome-wide average (trimmed of two extreme values among chromosomes for each position). The averages of individual chromosomes are shown as semi-transparent lines. **e**, Profiles of mouse hippocampus 10x Chromium dataset ($n = 18{,}213$). **f**, Profile for human forebrain 10x data ($n = 1{,}720$). **g**, Profile for the chromaffin differentiation data measured using SMART-seq2 ($n = 385$). **h**, Profile for the mouse bone marrow data measured using inDrop ($n = 3{,}018$). The top left corner of each plot shows the number of all intronic reads (that is, falling within the gene, but not touching an exon) that falls within the 250 bp around internal priming sites (1,500 bp was used for the SMART-seq2 dataset). In 10x data, while concordant internal priming sites produce stronger signal, their frequency within the genome is lower than those of discordant sites, so that overall discordant sites account for slightly higher fraction of intronic signals. By contrast, the inDrop dataset appears to have very limited discordant priming.

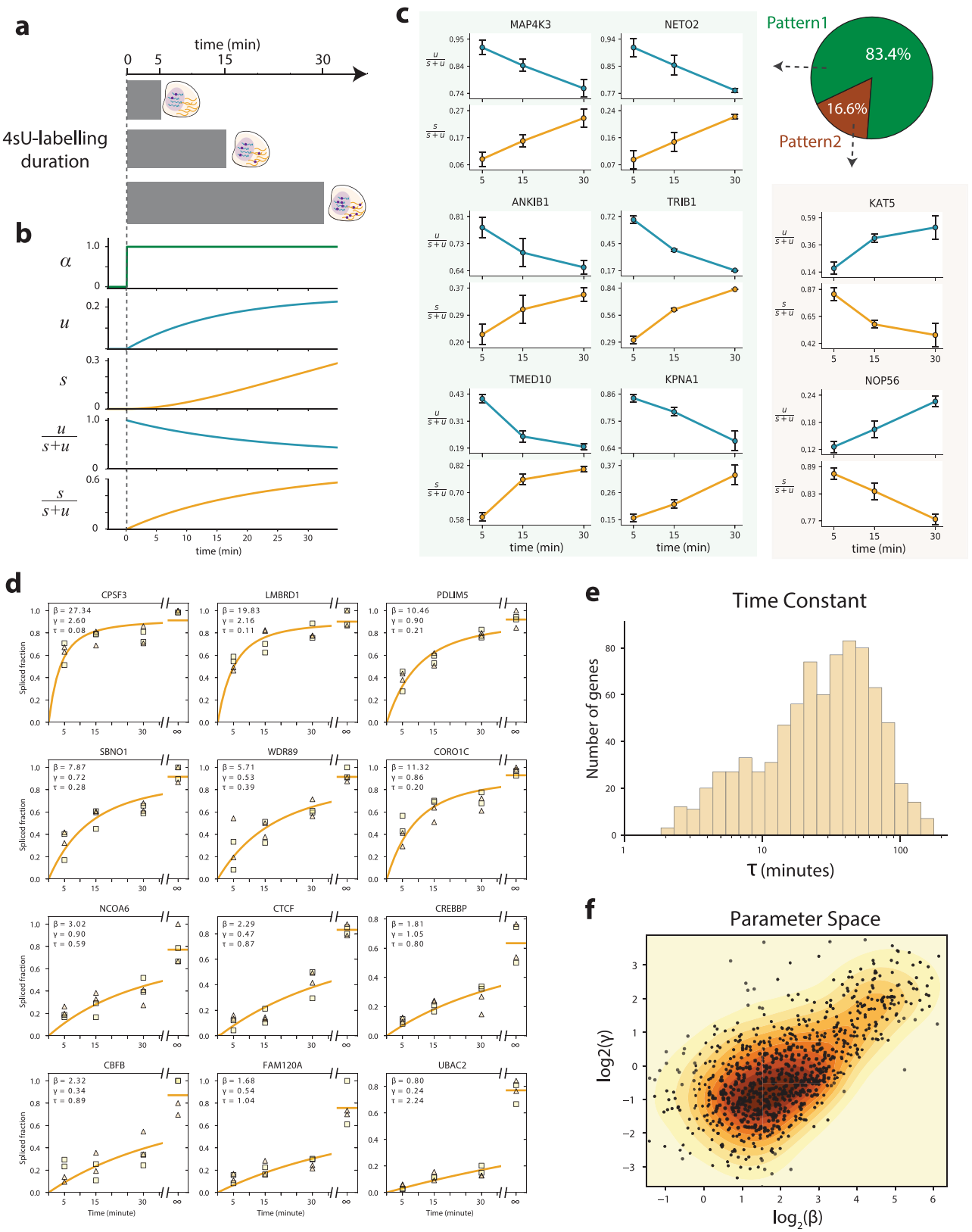

Extended Data Fig. 2 | Estimation of the characteristic time of RNA metabolism in human cells. a, Design of the metabolic labelling experiment in human cells. HEK293 cells were exposed to 4-thiouridine (4sU) for 5, 15 or 30 min, and the labelled fraction was isolated and analysed. A no pull-down control was also analysed, and represents the equilibrium state (indicated by ∞). **b**, Expected profiles of the abundance and fraction of labelled spliced and unspliced RNA molecules. **c**, The observed dynamic profiles of genes were clustered, yielding two groups: the majority (83.4%) were concordant with the expectation of increasing labelling; and a smaller fraction (16.6%) of discordant genes. Bars indicate s.e.m. $n_{genes} = 998$, $n_{technical} = 2$, $n_{biological} = 2$. **d**, Curves showing maximum likelihood fit to the data, based on the analytical solution for a step increase in the transcription rate. The fit yields values of β and γ, and of the characteristic time constant τ, defined as the time required to reach $1 - 1/e \approx 63.2\%$ of the asymptotic value. **e**, The distribution of τ values. **f**, The joint distribution of the fit β and γ parameters ($n = 832$).

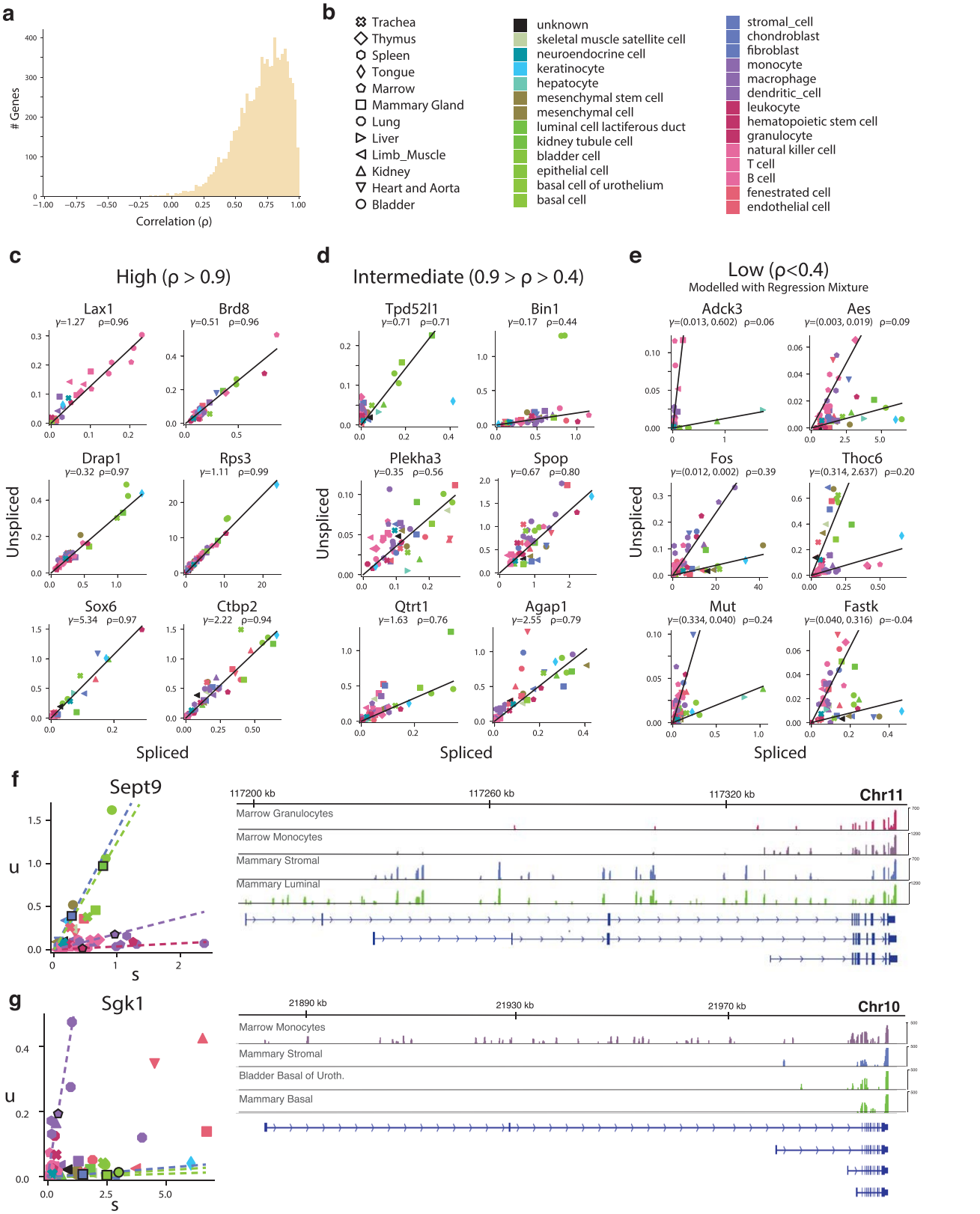

Extended Data Fig. 3 | Degradation rates are conserved over a wide range of terminally differentiated cell types. Conservation of the RNA degradation rate over a wide range of different cell types in the adult mouse (Tabula Muris dataset). **a**, The distribution over the genes of the correlation of spliced and unspliced molecule counts across all the cell types ($n_{genes} = 8{,}385$). **b**, Legend enumerating the tissues and cell classes annotated by the Tabula Muris consortium ($n = 48$). Functionally, developmentally or phenotypically related classes are coloured with similar colours to aid the interpretation of the plots below. **c**, **d**, A representative selection of genes with high correlation ($\rho > 0.9$) (**c**) and typical correlation ($0.9 > \rho > 0.4$) (**d**). γ was estimated by robust linear regression (RANSAC). **e**, Plots show a selection of genes displaying two clearly distinct degradation rates (such genes with double γ amounted to 10.8% of the total). The values of the two different γ were estimated by regression mixture modelling. **f**, **g**, Two examples of genes where multiple values of γ are explained by alternative splicing in different cell types.

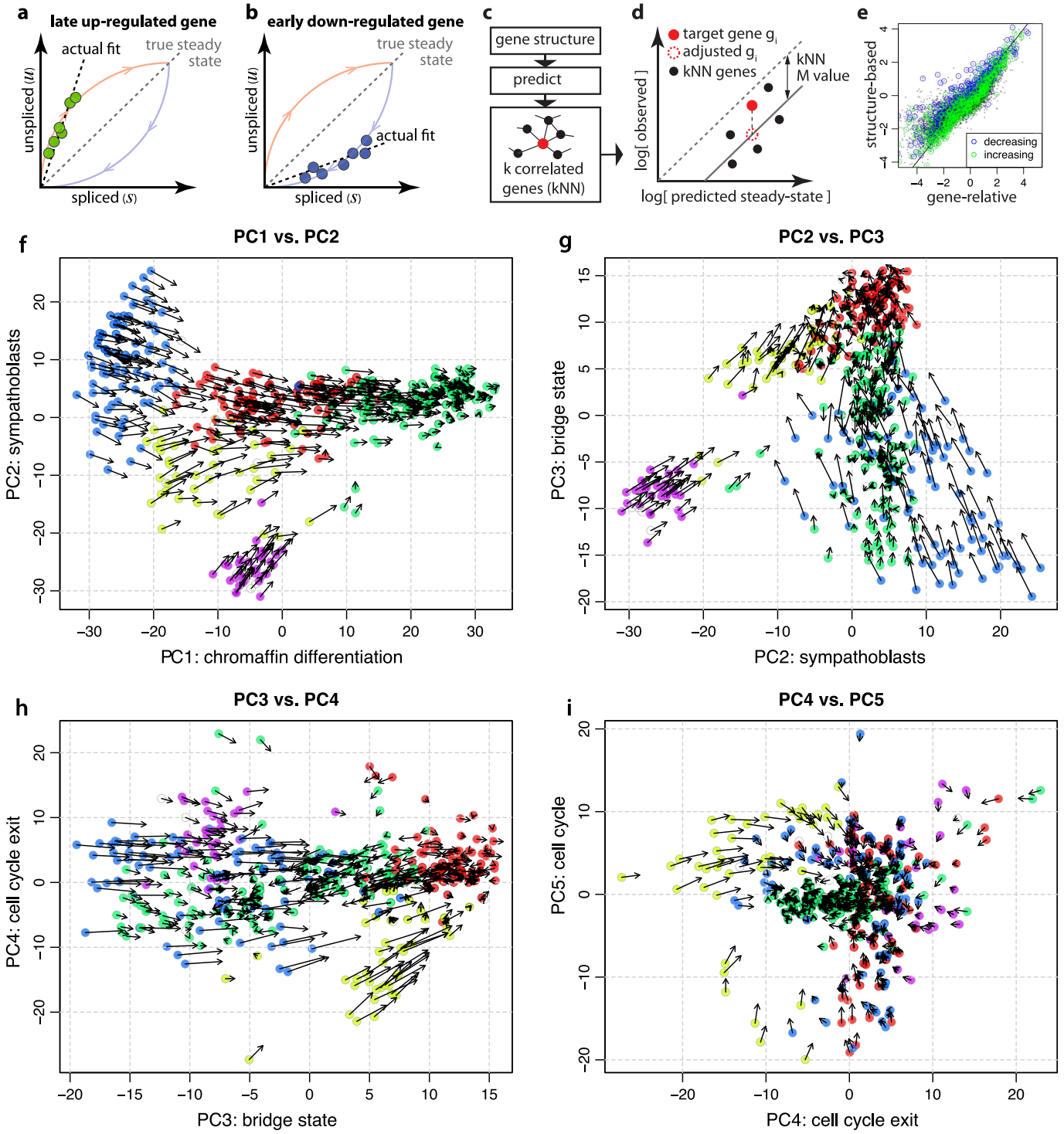

Extended Data Fig. 4 | Structure-based velocity estimation. a, **b**, For genes that are observed only outside of the steady state, such as genes upregulated late in the chromaffin differentiation (**a**) or downregulated early in the Schwann cell precursors (**b**), gene-relative γ fit is likely to deviate from its steady-state value. **c**, **d**, To correct for such effects, a structure-based γ fit will first predict γ for every gene based on its structural parameters, and then use the k most correlated genes in the dataset to adjust M value ($M = \log_2(u_o/u_{ss})$, where u_{ss} is the unspliced counts predicted from spliced counts under steady-state, and u_o is the observed unspliced count) using robust mean, and re-estimate γ. **e**, Scatter plot comparing gene-relative and structure-based γ estimates, with coloured circles highlighting γ adjustments for genes downregulated early in SCPs (blue) and upregulated late in chromaffin cells (green). The values are shown on a natural log scale. **f**–**i**, Cell expression velocity in the chromaffin E12.5 dataset, based on the structure-based γ estimates, shown on the first five PCs.

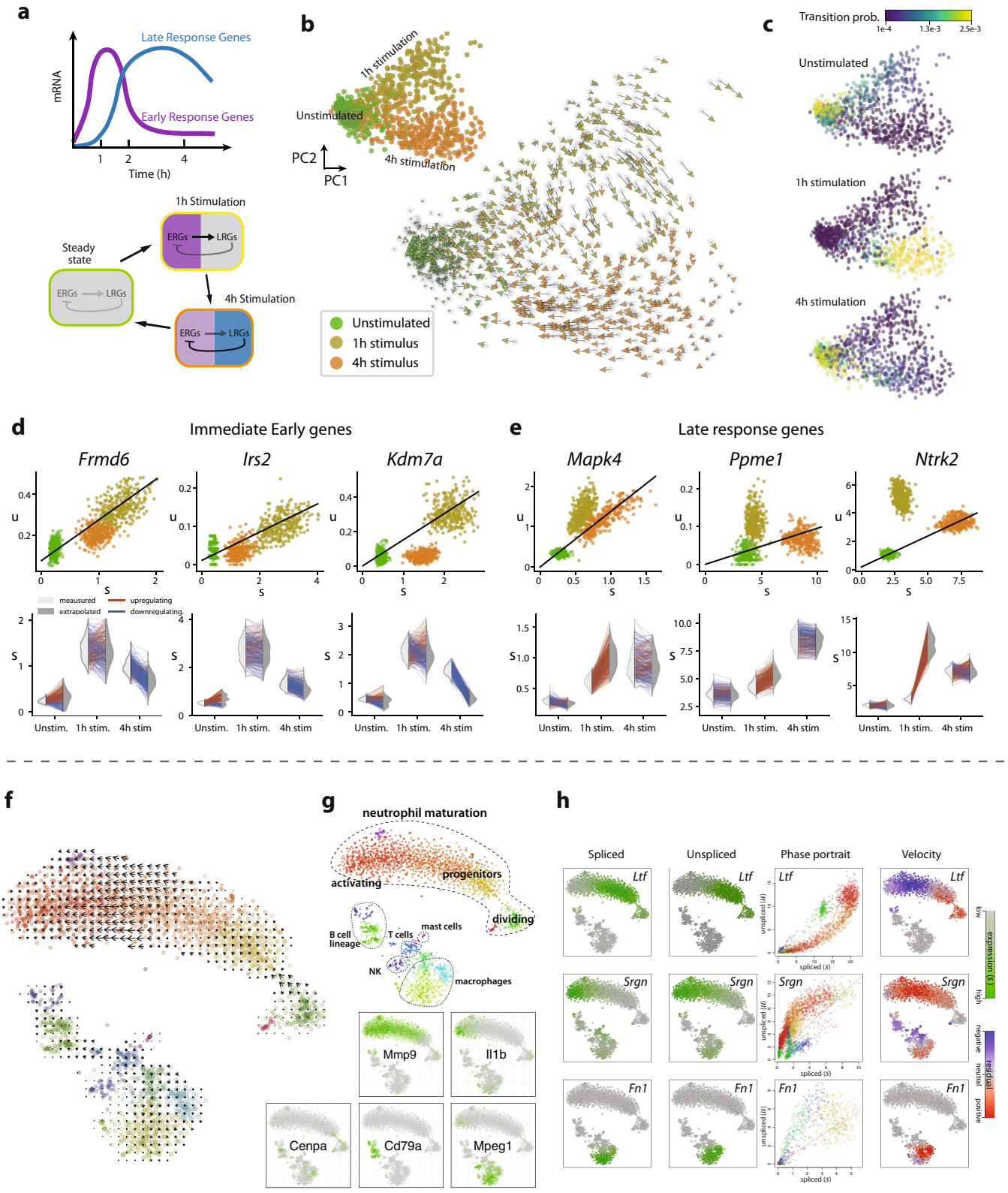

Extended Data Fig. 5 | See next page for caption.

Extended Data Fig. 5 | RNA velocity analysis of inDrop datasets: visual stimulus response of cortical pyramidal neurons and neutrophil differentiation. **a**, Simplified illustration of a model of activation of pyramidal neurons of the visual cortex after exposure to a light stimulus. **b**, Velocity estimates projected onto a two-dimensional PCA plot of the dataset ($n = 952$). **c**, Average transition probability of unstimulated cells (top), cells stimulated for 1 h (middle) and cell stimulated for 4 h (bottom). The unstimulated cells mostly were stationary and only few cells show the tendency of activating early response genes (probably as a result of the dissociation procedure). Cells stimulated for 1 h were characterized by expressing immediate early genes and high velocity in late response genes, and they were, therefore, transitioning to a state more similar to the one observed for the 4-h activation time point. After 4 h of stimulations cells appeared to be reverting to a state comparable to the unstimulated sample (bottom). **d**, **e**, Top panels, phase portraits of early (**d**) and late (**e**) response genes. Bottom panels, violin plots show expression distribution over the cell population at each time point (left half of the violin) and extrapolation to the future using velocity (right half of the violin). In the plot, transitions of single cells are indicated by lines connecting the two halves of the violins and coloured by the sign of the velocity of each gene. **f**, Grid visualization shows cell expression velocity estimates for the inDrop mouse bone marrow dataset on a *t*-SNE plot ($n = 3{,}018$). **g**, Major cell populations are labelled based on manual annotation. The velocity flow in **a** captures neutrophil maturation, starting from the dividing cells on the right, all the way to *Il1b* activation on the left. Expression profiles for five marker genes are shown below. **h**, The plots illustrate gene-relative model fits for several example genes. For each gene, the first column shows spliced molecular counts in different cells. The second column shows unspliced molecular counts. The third column shows phase portrait of a gene (unspliced versus spliced dependency) and the resulting γ fit (dashed red line), as determined using extreme quantile method. Each point corresponds to a cell, coloured according to cluster labels shown in **g**. The last column shows unspliced count signal residual based on the estimated γ fit, with positive residuals indicating expected upregulation, and negative residuals indicating expected downregulation of a gene.

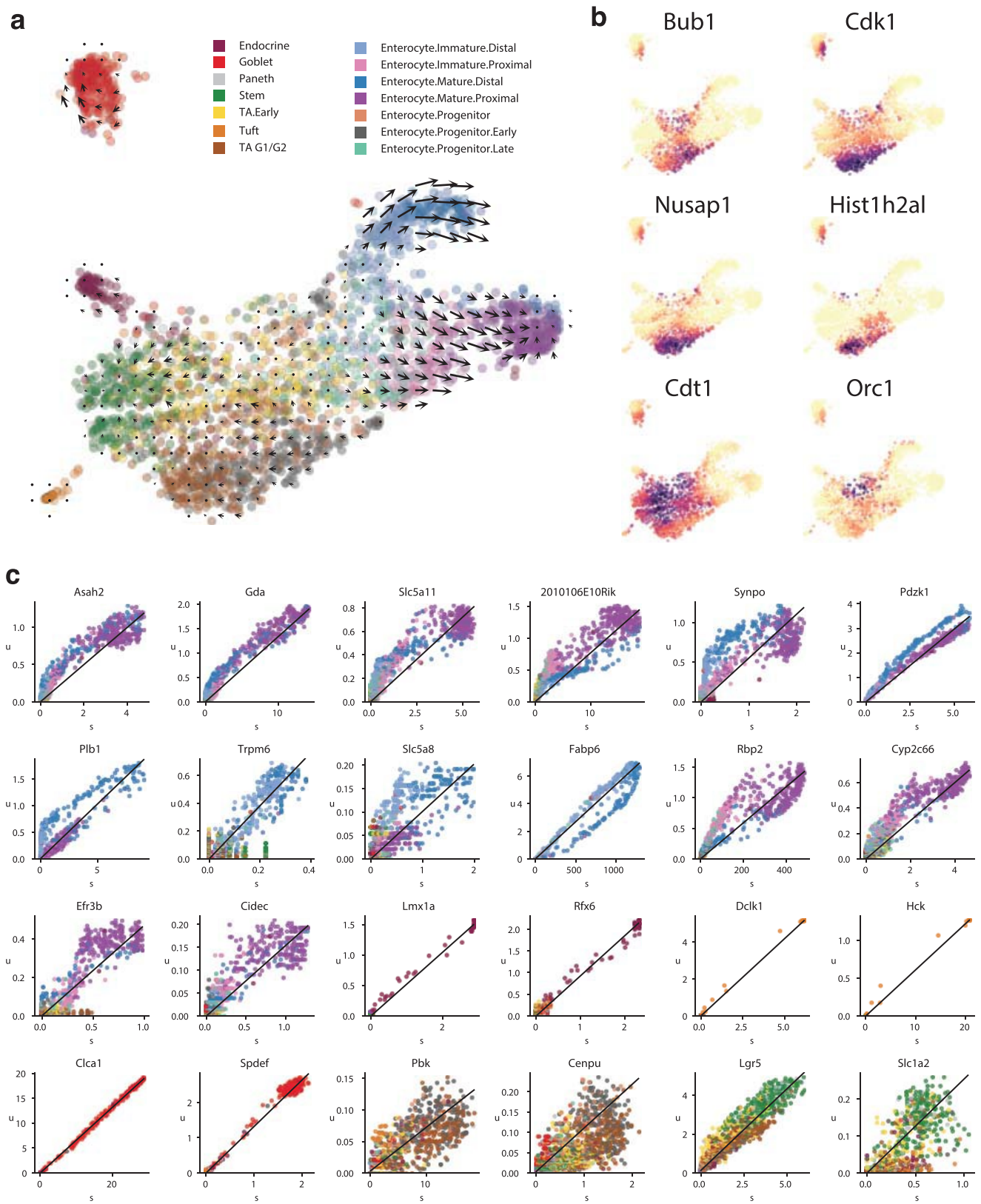

Extended Data Fig. 6 | See next page for caption.

Extended Data Fig. 6 | Dynamics of maturation of enterocytes during intestinal homeostasis. a, Velocity field projected on a 2D *t*-SNE plot. The clusters are labelled and coloured as in the original publication[11] to facilitate comparison ($n = 2{,}683$). Velocity analysis revealed a transition related to the maturation of distal and proximal enterocytes. No consistent velocity was observed in the part of the manifold occupied by stem cells and transit amplifying (TA) cells, suggesting that stem cell dynamics are more difficult to capture either for their slower rate or a more stochastic nature. The small velocities of transit amplifying cells were likely to be driven by the cell cycle. **b**, A selection of the cell cycle genes that were removed from the analysis is plotted on the *t*-SNE. Despite the removal of the genes annotated as cell cycle genes, we still observed important segregation by cell cycle, illustrating the difficulty of disentangling cell cycle phase from the cell state. **c**, A selection of phase portraits that show genes underlying the observed velocity field. Markers of endocrine, goblet and tuft cells displayed no detectable velocity. Velocity towards and from stem cell states was detectable for a limited set of genes (such as the stem cell marker *Lgr5*), however, on the genome-wide level, the exact dynamics of this process was probably confounded by the high correlation with cell cycle.

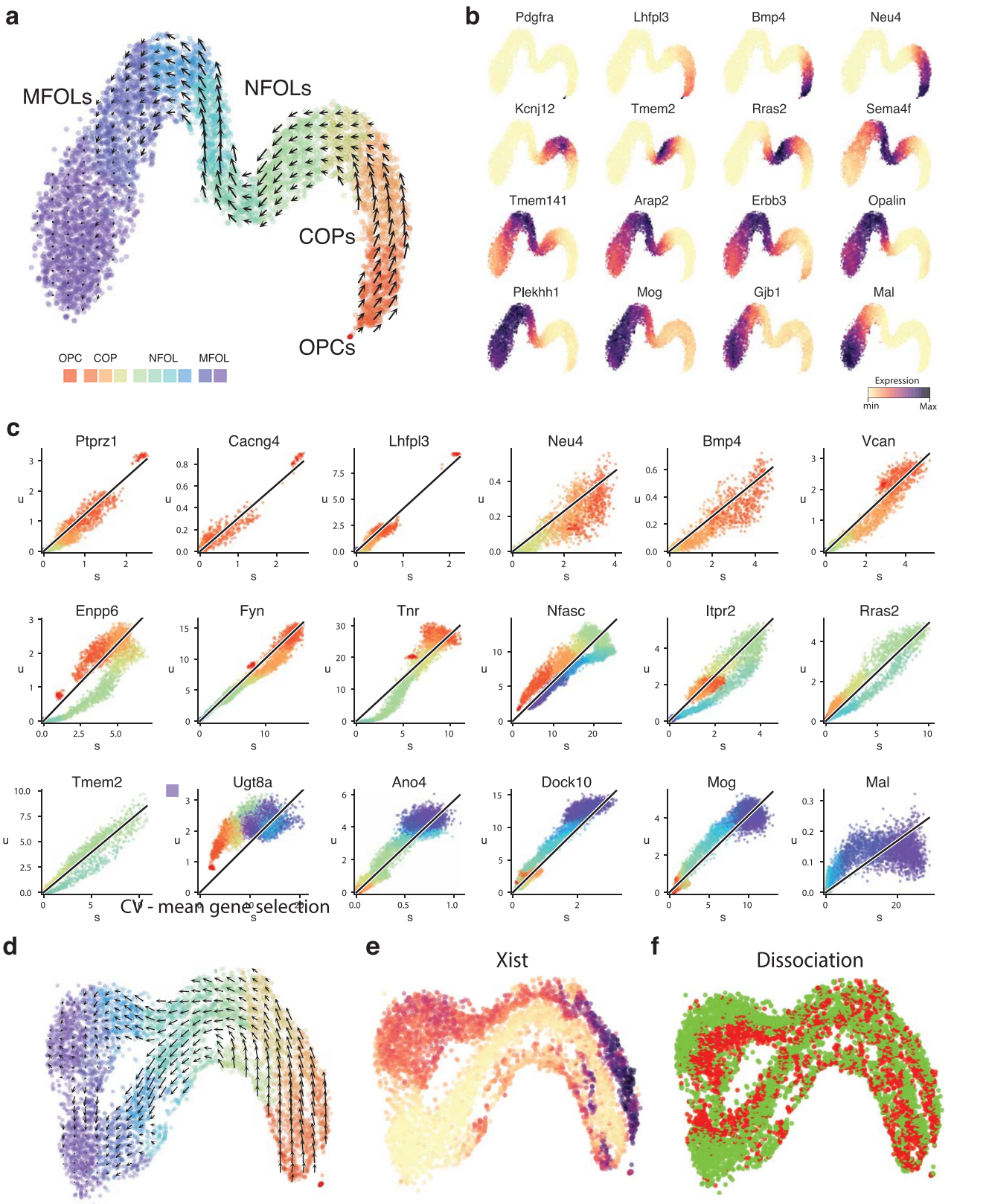

Extended Data Fig. 7 | See next page for caption.

Extended Data Fig. 7 | RNA velocity unveils the dynamics of differentiation and myelination of oligodendrocytes. a, *t*-SNE projection shows the landscape of oligodendrocyte lineage differentiation and myelination process in the hindbrain (pons) of adolescent (P20) mice ($n = 6{,}307$). The velocity field reflects the dynamics of expression of both the initial differentiation wave and the following expression changes associated with the myelination process. The cell clusters are coloured by pseudotime as in **c** to facilitate interpretation. **b**, Expression patterns of landmark genes of the differentiation process. *Pdgfra* is the canonical marker of oligodendrocyte precursors (OPCs), *Neu4* marks committed oligodendrocyte precursors (COPs), *Tmem2* is enriched in newly formed oligodendrocytes (NFOLs) and the expression of *Mog* is upregulated at the beginning of the myelination process in myelin-forming oligodendrocytes (MFOLs). **c**, A selection of phase portraits underlying the velocity field shown in **a**. **d**, *t*-SNE projections and velocity vector field of the same dataset, but analysed using a more naive feature selection that has retained other axes of variation on top of the oligodendrocyte maturation (sex and day of dissection). Notice that despite the separation of populations into $Xist^{+}$ and $Xist^{-}$ tracks, the velocity field correctly captures progression from progenitors to newly formed oligodendrocytes in the two parallel tracks. **e**, Level of expression of *Xist* showing that most of the extra variation is driven by the sex of the animal. **f**, Cells coloured by the day on which the experiment was performed.

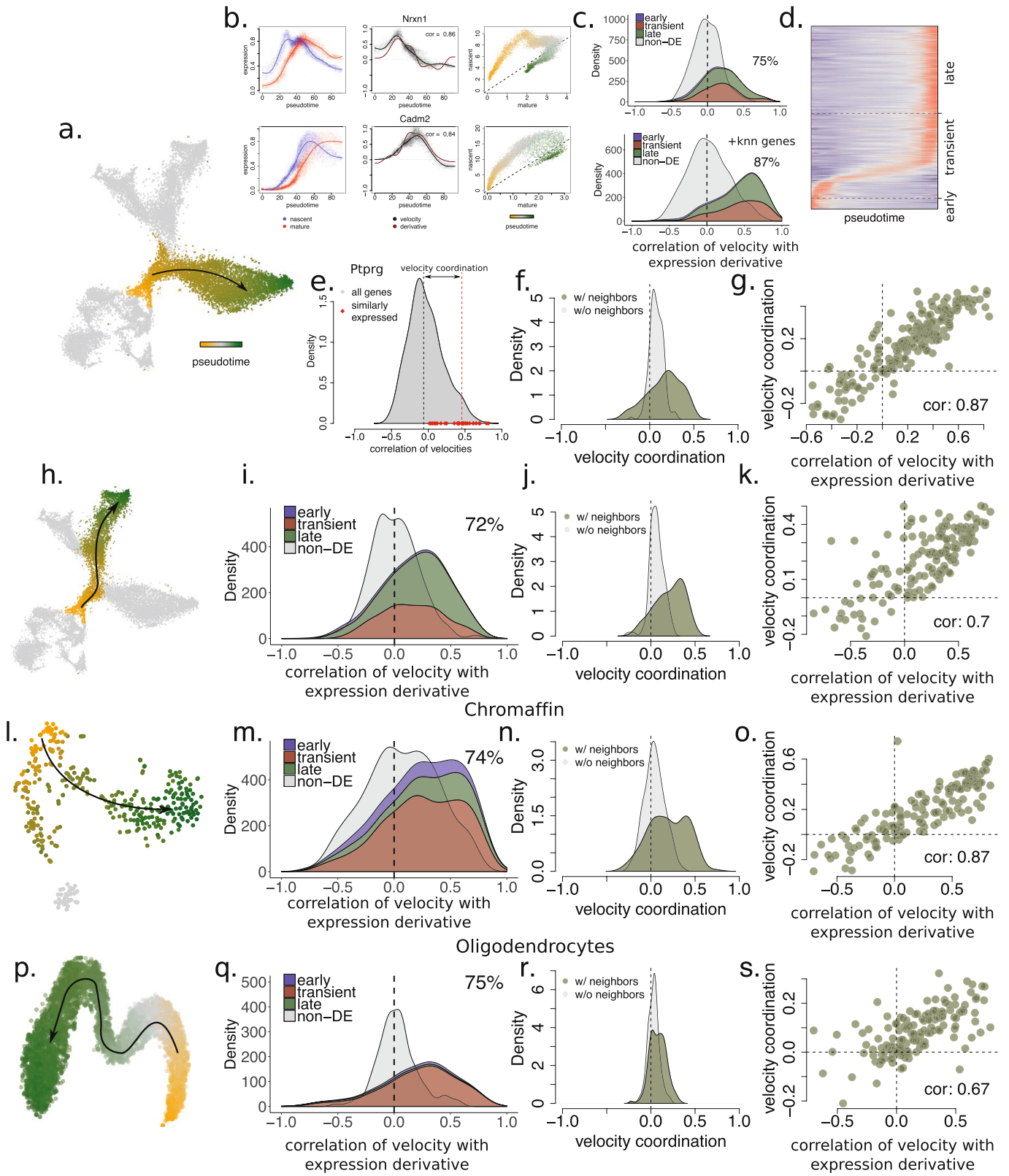

Extended Data Fig. 8 | See next page for caption.

Extended Data Fig. 8 | Agreement of velocity predictions with the observed expression derivatives. a, Maturation progression of granule neurons in the mouse hippocampus dataset is approximated by pseudotime (estimated with a principal curve). **b**, For a pair of example genes (rows), the plots show unspliced and spliced gene expression profiles along the pseudotime (left panels), empirically estimated smoothed pseudotime derivative of the observed gene expression and the estimated RNA velocity (middle panels), as well as the relationship between spliced and unspliced expression (right panel). The velocity estimates for the two chosen genes are highly correlated with the empirically observed derivative, indicating accurate velocity estimation. **c**, The majority (75%) of the genes that were differentially regulated along the pseudotime trajectory showed a positive correlation with the empirical expression derivative. The distribution of such genes is split according to three classes of trajectory-associated genes as shown in **d**. By contrast, velocity estimates for genes that were not differentially expressed along the pseudotime trajectory did not show such correlation (grey). Incorporating information about co-regulated genes into velocity estimation using gene *k*NN clustering (see Supplementary Note 1) can significantly boost the accuracy of the velocity predictions (lower panel). **d**, Trajectory-associated genes were classified as early, transient and late, according to their peak expression time. *x* axis, cells ordered by pseudotime; *y* axis, genes ordered by their peak expression time. **e**, The genes that were well-correlated in terms of their spliced expression patterns with *Ptprg*, also showed a high correlation of their velocity estimates with *Ptprg*. To assess the degree of consistency of the velocities of co-regulated genes, we introduced a measure of velocity coordination for a given gene, as a difference between the mean correlations of the velocity estimates of the co-regulated genes and the velocity estimates of all genes. The two quantities being compared are shown for *Ptprg* with dotted vertical lines: grey, mean velocity correlation with all genes; red, mean velocity correlation with top co-regulated genes. Velocity coordination provides an unbiased measure of quality for velocity estimates. **f**, Velocities of co-regulated genes were correlated. Distribution of gene velocity coordination values is shown for genes that had co-regulated genes (that is, the genes that had well-correlated gene neighbours in terms of their spliced expression pattern, green), as well as for the genes that did not have enough co-regulated genes (without neighbours, grey). **g**, Co-regulated genes that had high velocity coordination tended to have high correlation with the empirical derivatives. Spearman correlation coefficient is shown. **h**–**k**, Velocity performance during maturation of pyramidal neurons (**h**). Genes differentially expressed during maturation had high correlation of velocity with empirical derivative (**i**), co-regulated genes tended to have correlated velocity estimates (**j**) and the degree of velocity coordination was associated with its correlation with empirical derivative (**k**). **l**, **m**, Velocity performance during chromaffin differentiation. **p**–**s**, Velocity performance during maturation of oligodendrocytes. Number of top co-regulated genes analysed for velocity correlation: 200 (**g**), 150 (**k**, **o**, **s**).

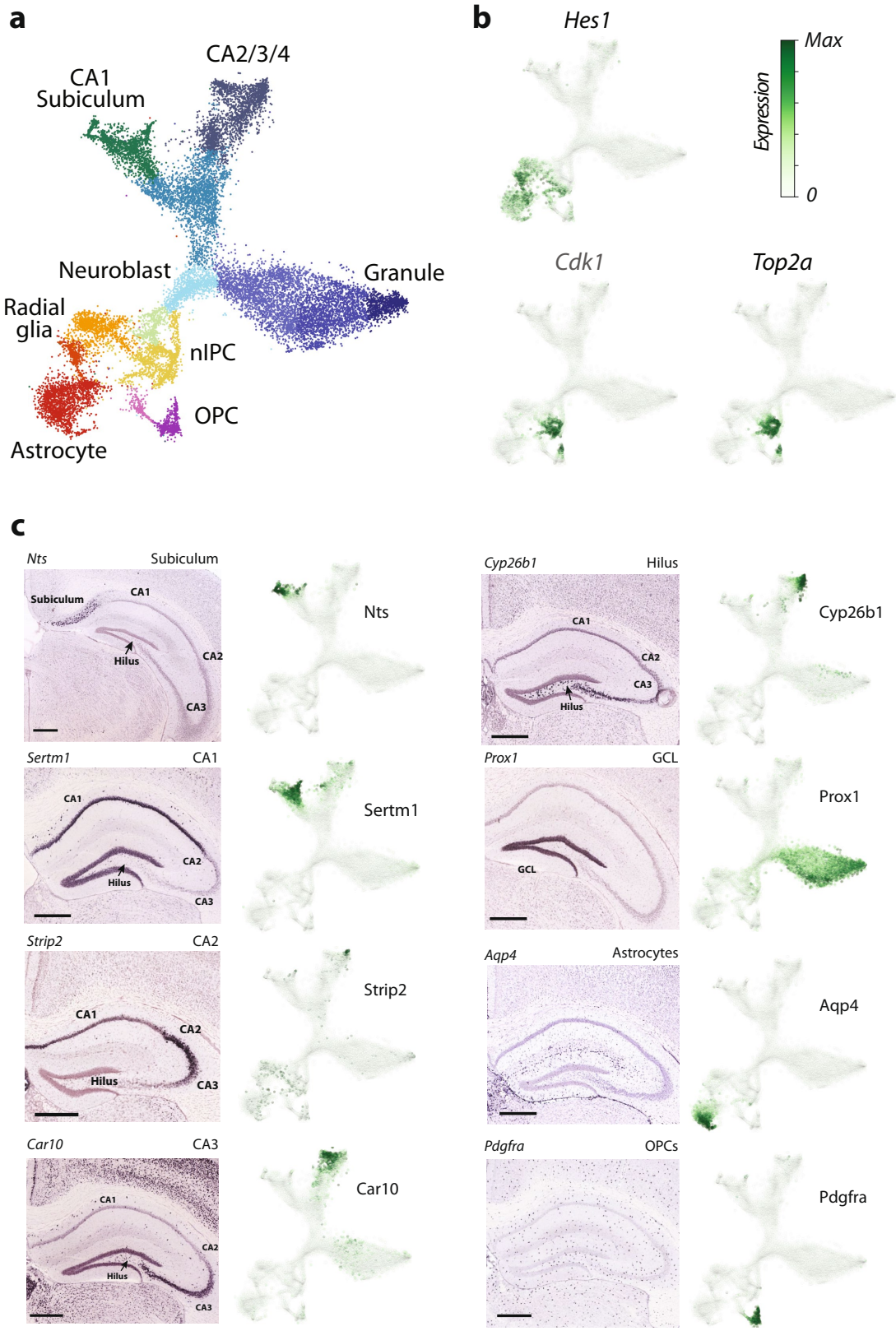

Extended Data Fig. 9 | Branching developmental trajectories of developing hippocampus. a, *t*-SNE plot of the developmental dentate gyrus dataset. Cells are coloured by cluster identities, with labels shown for the major cell types. **b**, Expression of radial glia (and astrocyte) marker *Hes1*, and cell cycle genes *Top2a* and *Cdk1* shown on the *t*-SNE plot. **c**, Marker genes of different regions of the hippocampus (in situ hybridization images from Allen Mouse Brain Atlas[24] show prominent expression signals at different extremities of the branching plot. Scale bars, 0.5 mm.

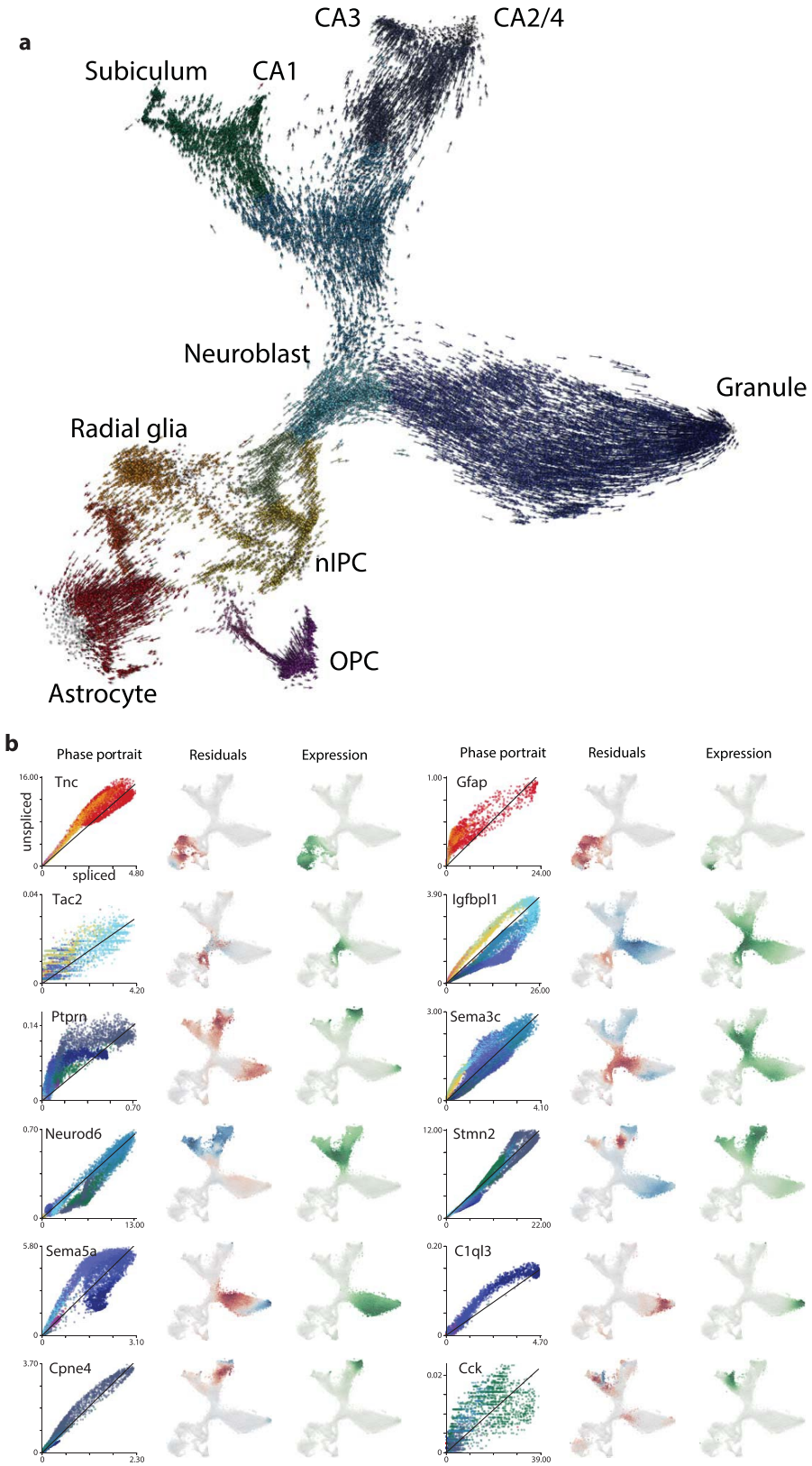

Extended Data Fig. 10 | Single-cell velocity estimates for individual cells in the embryonic hippocampus dataset. a, Arrows indicate the extrapolated state projected onto the *t*-SNE plot of the manifold. **b**, Selected phase portraits and fits of the equilibrium slope (γ) for the developing cells in the embryonic hippocampus dataset. For each gene, the first column shows spliced–unspliced phase portrait. The dashed line shows the γ fit. The second column illustrates the magnitude of the residuals (that is, the difference between observed and expected unspliced abundance, which closely tracks with velocity) for several genes involved in the development of different neural lineages. The third column shows the observed expression profile for spliced molecules.

nature research

Corresponding author(s): Peter Kharchenko and Sten Linnarsson

Reporting Summary

Nature Research wishes to improve the reproducibility of the work that we publish. This form provides structure for consistency and transparency in reporting. For further information on Nature Research policies, see Authors & Referees and the Editorial Policy Checklist.

Statistical parameters

When statistical analyses are reported, confirm that the following items are present in the relevant location (e.g. figure legend, table legend, main text, or Methods section).

n/a	Confirmed	
☐	☒	The exact sample size (*n*) for each experimental group/condition, given as a discrete number and unit of measurement
☐	☒	An indication of whether measurements were taken from distinct samples or whether the same sample was measured repeatedly
☐	☒	The statistical test(s) used AND whether they are one- or two-sided *Only common tests should be described solely by name; describe more complex techniques in the Methods section.*
☐	☒	A description of all covariates tested
☐	☒	A description of any assumptions or corrections, such as tests of normality and adjustment for multiple comparisons
☐	☒	A full description of the statistics including central tendency (e.g. means) or other basic estimates (e.g. regression coefficient) AND variation (e.g. standard deviation) or associated estimates of uncertainty (e.g. confidence intervals)
☐	☒	For null hypothesis testing, the test statistic (e.g. *F*, *t*, *r*) with confidence intervals, effect sizes, degrees of freedom and *P* value noted *Give P values as exact values whenever suitable.*
☒	☐	For Bayesian analysis, information on the choice of priors and Markov chain Monte Carlo settings
☒	☐	For hierarchical and complex designs, identification of the appropriate level for tests and full reporting of outcomes
☐	☒	Estimates of effect sizes (e.g. Cohen's *d*, Pearson's *r*), indicating how they were calculated
☒	☐	Clearly defined error bars *State explicitly what error bars represent (e.g. SD, SE, CI)*

Our web collection on statistics for biologists may be useful.

Software and code

Policy information about availability of computer code

Data collection	Nikon NIS Elements and 10X Genomics Cellranger 2.1.1 packages were used in acquiring experimental data.
Data analysis	The software is available under open source license in github repository, together with multiple analysis notebooks, at velocyto.org.

For manuscripts utilizing custom algorithms or software that are central to the research but not yet described in published literature, software must be made available to editors/reviewers upon request. We strongly encourage code deposition in a community repository (e.g. GitHub). See the Nature Research guidelines for submitting code & software for further information.

Data

Policy information about availability of data

All manuscripts must include a data availability statement. This statement should provide the following information, where applicable:

- Accession codes, unique identifiers, or web links for publicly available datasets
- A list of figures that have associated raw data
- A description of any restrictions on data availability

The data is available from short read sequencing archive, with accession numbers provided in the text.

Field-specific reporting

Please select the best fit for your research. If you are not sure, read the appropriate sections before making your selection.

☒ Life sciences ☐ Behavioural & social sciences ☐ Ecological, evolutionary & environmental sciences

For a reference copy of the document with all sections, see nature.com/authors/policies/ReportingSummary-flat.pdf

Life sciences study design

All studies must disclose on these points even when the disclosure is negative.

Sample size	sample size of each measurement was determined by the practical limitations of the protocol utilized. No statistical estimation of sample size was performed.
Data exclusions	cell types unrelated to the neurogenesis branches being analyzed were excluded from the final analysis, as described in the Methods. (however full dataset has been made available).
Replication	the approach was applied to multiple independent datasets, as presented in the manuscript. Multiple batches or timepoints served as replicates (showing consistency in all dataset). Similarly, the approach is implemented by two distinct pipelines (python and R version), which for a computational idea, served as another type of replication. In the analysis of the embryonic adrenal medulla, sample size was between 3-6 embryos derived from 1 to 2 independent litters to ensure reproducibility.
Randomization	bootstrap sampling across cells and genes was performed to assess sensitivity of results on individual datasets. Samples were not randomized across experiments.
Blinding	blinding is not applicable to the described experimental designs (i.e. single-cell measurements of a known normal tissue).

Reporting for specific materials, systems and methods

Materials & experimental systems

n/a	Involved in the study
☒	☐ Unique biological materials
☒	☐ Antibodies
☒	☐ Eukaryotic cell lines
☒	☐ Palaeontology
☐	☒ Animals and other organisms
☐	☒ Human research participants

Methods

n/a	Involved in the study
☒	☐ ChIP-seq
☒	☐ Flow cytometry
☒	☐ MRI-based neuroimaging

Animals and other organisms

Policy information about studies involving animals; ARRIVE guidelines recommended for reporting animal research

Laboratory animals	For the oligodendrocyte dataset, we used male and female mice of the CD1 strain at postnatal days 20, 21 and 22. In the analysis of the embryonic adrenal medulla, wild type CD1 mice or transgenic Htr3a-EGFP mice were used (received from MMRRC and provided by J. Hjerling-Leffler laboratory (Karolinska Institutet, Sweden) (https://www.mmrrc.org/catalog/sds.php?mmrrc_id=273).
Wild animals	study did not involve wild animals.
Field-collected samples	study did not involve field-collected samples

Human research participants

Policy information about studies involving human research participants

Population characteristics	Human first trimester subcortical forebrain tissue was obtained from elective routine abortions (10 weeks postconception) with the written informed consent of the pregnant woman and in accordance with the ethical permit given by the Regional Ethics Vetting Board (Stockholm, Sweden). Human fetal forebrain tissue was collected and stored in hibernation media with addition of GlutaMAX and B-27 supplements according to the manufacture's instructions (overnight, 4oC, Hibernate-A, Thermo-Fisher). The

tissue was then cut into small cubic pieces of approximately 1-2mm length. Tissue was dissociated using a dissociation kit (Miltenyi, Neural Tissue Dissociation Kit (P)) according to manufacture's instructions. In short, tissue was prepared in the kit buffer containing 0.067mM beta-mercaptoethanol. After addition of enzyme mix 1 and 2, the tissue was mechanically dissociated using three increasingly smaller gauges of fire polished Pasteur pipettes, pipetted 20, 15 and 10 times up and down respectively. Ultimately, collected cells were stored on ice in PBS containing 1% BSA and immediately prepared for single cell library preparation. Single-cell RNA sequencing was performed using the 10X Genomics Chromium V2 kit, following the manufacturer's protocol, and sequenced on an Illumina Hiseq 2500.

Recruitment

Participants were recruited as part of routine clinical elective abortions. Self-selection bias is unlikely to have affected the results, as the embryos derived from elective abortions are likely to be normal.